COMPUTATIONAL SCREENING OF MAIN GROUP HETEROGENEOUS CATALYSTS FOR CHEMICAL UPCYCLING

TU Delft

Computational Screening of Main-Group Heterogeneous Catalysts for Chemical Plastic Upcycling

by

Amer Alramdan

to obtain the degree of Master of Science in Chemical Engineering
at the Delft University of Technology

to be defended publicly on May 6, 2025

Performed at:
Inorganic Systems Engineering
Faculty of Applied Sciences

Student Number: 5688957
Project Duration: September 23, 2024 – 25 April, 2025

Supervisors:
Prof. Dr. Evgeny Pidko
Dr. Alexander Kolganov

Thesis Committee:

Prof. Dr. Evgeny Pidko, TU Delft, Applied Sciences

Prof. Ferdinand Grozema, TU Delft, Applied Sciences

Dr. Atul Bansode, TU Delft, Applied Sciences

ISEgroup
ChemE @ TU Delft

TU Delft Delft University of Technology

Contents

List of Figures iii

1 Introduction 1
1.1 Limitations of Conventional Plastic Disposal and Recycling . . . 1
1.1.1 Mechanical Recycling . . . 1
1.1.2 Chemical Recycling . . . 2
1.1.3 Comparison of Mechanical and Chemical Recycling . . . 3
1.2 Chemical Upcycling Pathways and Catalytic Approaches . . . 3
1.2.1 Pyrolysis . . . 3
1.2.2 Catalytic Pyrolysis . . . 4
1.2.3 Hydrogenolysis . . . 6
1.2.4 Catalytic upcycling on sulfated zirconium oxide . . . 6
1.3 Computational Approach and Thesis Objectives . . . 8

2 Theory 9
2.1 Density Functional Theory . . . 9
2.1.1 Exchange-Correlation Functional . . . 10
2.1.2 DFT+U: Addressing the Limitations of Standard DFT . . . 11
2.1.3 DFT-D Method . . . 11
2.1.4 K-Point Sampling, Plane Waves, and Pseudopotentials . . . 12
2.1.5 Potential Energy Surface . . . 12
2.2 Adsorption of Acids on ZrO_2 Surface . . . 14
2.2.1 Summary of Adsorption & Condensation . . . 14
2.3 Adsorption Energy Calculations . . . 14
2.4 Lewis Acidity and Probing Molecules . . . 14

3 Methods 15
3.1 Computational Setup . . . 15
3.1.1 Surface Model . . . 15
3.1.2 High-Performance Computing: Snellius Supercomputer . . . 15
3.1.3 VASP Input Files . . . 15
3.1.4 Geometry Optimization . . . 16
3.1.5 Molecular Visualization and Analysis Using Chemcraft . . . 16
3.2 Varying Proton Locations . . . 17
3.3 Surface Saturation . . . 18
3.4 Polypropylene activation studies . . . 19
3.5 Probing Lewis Acids . . . 19
3.5.1 Nudged Elastic Band . . . 20

4 Results & Discussion 22
4.1 Adsorption Energy of Acid Species . . . 22
4.2 Saturation Adsorption Energy . . . 23
4.3 Probing Lewis Acidity . . . 23
4.4 Hydride Abstraction: Reaction Energies and Kinetics . . . 23
4.4.1 NEB Calculations and Reaction Profiles . . . 24
4.5 Comparison of Screened Acids with Pyrosulfated Zirconia . . . 25

5 Conclusion & outlook 27

Bibliography 29

Appendices

A Varying proton locations 1
A.1 Coloring scheme . . . 1
A.2 Pyrophosphate on ZrO_2 . . . 1
A.3 Tetraboric acid on ZrO_2 . . . 2
A.4 Diboric acid on ZrO_2 . . . 3
A.5 Disulfuryl fluoride, Triflic acid anhydride, and Bistriflimide on ZrO_2 . . . 3
A.6 Adsorption energies. . . . 4

B Surface saturation 5
B.1 Coloring scheme . . . 5
B.2 Phosphoric acid. . . . 5
B.3 Tetraboric acid . . . 6
B.4 Boric acid . . . 6
B.5 Fluorosulfuric acid . . . 6
B.6 Triflic acid. . . . 7
B.7 Bistriflimide. . . . 7
B.8 Effect of surface saturation . . . 8

C Reactivity 9
C.1 Coloring scheme . . . 9
C.2 Phosphoric acid. . . . 9
C.3 Tetraboric acid . . . 10
C.4 Boric acid . . . 10
C.5 Fluorosulfuric acid . . . 11
C.6 Triflic acid. . . . 11
C.7 Tetraboric acid (reorganized) . . . 12
C.8 Reaction energies . . . 12

D Probing lewis acids 13
D.1 Coloring scheme . . . 13
D.2 Phosphoric acid. . . . 13
D.3 Tetraboric acid . . . 14
D.4 Boric acid . . . 14
D.5 Fluorosulfuric acid . . . 15
D.6 Triflic acid. . . . 15

E Artificial Intelligence 16
E.1 Literture search . . . 16
E.2 Language Refinement and Scientific Writing Assistance . . . 16
E.3 Scientific Concept Clarification . . . 17
E.4 Scripting and Automation. . . . 17

F INCAR tags 18

List of Figures

1.1 Global plastic production: According to Organisation for Economic Cooperation and Development (OECD) projections, the figure shows the expected exponential growth in plastic production over the next forty years [6]. 1
1.2 Radical formation during the mechanical recycling of common plastics. Mechanical stress and heat generate radicals along polymer chains, such as in PET, PS, PE, PP, and PVC. These radicals may undergo hydrogen abstraction followed by β-scission, leading to chain cleavage [13]. 2
1.3 Overview of chemical recycling pathways, including monomer recovery and catalytic upcycling. Catalytic upcycling enables selective polymer breakdown into high-value chemical intermediates rather than direct monomer regeneration [18]. 3
1.4 Effect of pyrolysis temperature on liquid yield (wt.%) PE and PP [32]. 4
1.5 Simplified mechanism of zeolite-catalyzed hydrocarbon cracking. The catalyst activates the alkane by protonation or hydride removal, forming a reactive carbenium ion. This ion undergoes β-scission, breaking carbon-carbon bonds to form smaller molecules. The cycle continues, producing lighter products through repeated cracking steps[40]. 5
1.6 General hydrogenolysis mechanism over metal catalysts. Polymer chains adsorb to the metal surface, and undergo dehydrogenation, followed by C–C bond cleavage and rehydrogenation to form shorter saturated hydrocarbons[42]. 6
1.7 C–H bond activation on sulfated ZrO_2, showing pyrosulfate bond cleavage, transient SO_3 formation, and hydride abstraction leading to carbocation generation [46]. 7
1.8 Lewis acidity probes used in the work of Jammee et al. 7
1.9 Reaction profile for sulfated zirconia (SZO) from the work of Jammee et al. 8
1.10 (a) H_3PO_4 (Phosphoric acid), (b) $H_2B_4O_7$ (Tetraboric acid), (c) H_3BO_3 (Boric acid), (d) $HFSO_3$ (Fluorosulfuric acid), (e) CF_3SO_3H (Triflic acid), and (f) $(CF_3SO_2)_2NH$ (Bis-triflimide). Bond distances are given in angstroms (Å). 8

2.1 Jacob's Ladder of DFT functionals, illustrating the hierarchy from LDA to hybrid functionals [53]. 11
2.2 PES showing ground state (minimum) and transition state (maximum) [57]. 13
2.3 Schematic representation of a potential energy surface (PES), showing reactants, products, intermediates, and transition states along the minimum energy path (MEP) [58]. 13
2.4 Probing molecules used to evaluate interaction energy. (a) CO (b) Pyridine (c) TEPO. 14

3.1 POSCAR file of Pyrophosphated Zirconia, showing lattice vectors, atomic species, atom counts, and cartesian coordinates with selective dynamics. 16
3.2 Schematic representation of the SCF algorithm used for geometry optimization in VASP[68]. . . 16
3.3 Colouring scheme used in the presentation of structures. 17
3.4 Side view of t-ZrO_2(101) surface. 17
3.5 Varying proton locations for pyrophosphate adsorbed on the ZrO_2 surface. The top row shows schematic representations with bond lengths (Å), while the bottom row presents corresponding 3D structures. 18
3.6 Saturation of ZrO_2 surface with phosphoric acid. Three $HPO_4{}^{2-}$ species were added, leading to eight total surface protons. 19
3.7 (Left) Initial state with trimer on top. (Right) Final state after hydride abstraction. 19
3.8 Interaction of TEPO, CO, and Pyridine with the Lewis acid site. 20
3.9 Illustration of the NEB method, showing interpolated images along the reaction path and the transition state at the energy maximum. Spring forces maintain a uniform distribution of images along the path [71]. 20
3.10 Comparison of Regular NEB and CI-NEB, highlighting CI-NEB's improved accuracy in locating the true transition state [73]. 21

4.1 Adsorption energies of acid molecules on the ZrO_2 surface. 22
4.2 (a) Tetraborate (B_4O_7) remains intact. (b) Zr and O sites are more exposed. Borate cluster is distorted. Borate shifts downward, forming new Zr-O coordination. 24
4.3 Fluorosulfuric acid reaction profile 24
4.4 Phosphoric acid reaction profile 25
4.5 Triflic acid reaction profile 25

A.1 Colouring scheme used in the presentation of structures. 1
A.2 Varying proton locations for pyrophosphate adsorbed on the ZrO_2 surface. The top row shows schematic representations with bond lengths (Å), while the bottom row presents corresponding 3D structures. 1
A.3 Varying proton locations for tetraboric acid adsorbed on the ZrO_2 surface. The top row shows schematic representations with bond lengths (Å), while the bottom row presents corresponding 3D structures. 2
A.4 Varying proton locations for diboric acid adsorbed on the ZrO_2 surface. The top row shows schematic representations with bond lengths (Å), while the bottom row presents corresponding 3D structures. 3
A.5 structure of (a) Disulfuryl fluoride, (b) Triflic acid anhydride, and (c) Bistriflimide on ZrO_2. The top row shows schematic representations with bond lengths (Å), while the bottom row presents corresponding 3D structures. 3

B.1 Colouring scheme used in the presentation of structures. 5
B.2 Saturation of pyrophosphated zicronia. Three $HPO_4{}^{2-}$ species were added, leading to eight total surface protons. 5
B.3 one additional tetraboric was adsorbed, leading to four total surface protons. 6
B.4 saturation of diboric acid on ZrO_2. Three $HBO_3{}^{2-}$ species were added, leading to eight total surface protons. 6
B.5 saturation of disulfuryl fluoride on ZrO_2. Three $SFO_3{}^-$ species were added, leading to three total surface protons. 6
B.6 saturation of triflic anhydride on ZrO_2. Three $CF_3SO_3{}^-$ species were added, leading to three total surface protons. 7
B.7 one additional bistriflimide was adsorbed, leading to two surface protons. 7
B.8 Adsorption energies (eV) of various acids before (red) and after (blue) surface saturation. 8

C.1 Colouring scheme used in the presentation of structures. 9
C.2 (Left) Initial state with trimer on top. (Right) Final state after hydride abstraction. 9
C.3 (Left) Initial state with trimer on top. (Right) Final state after hydride abstraction. 10
C.4 (Left) Initial state with trimer on top. (Right) Final state after hydride abstraction. 10
C.5 (Left) Initial state with trimer on top. (Right) Final state after hydride abstraction. 11
C.6 (Left) Initial state with trimer on top. (Right) Final state after hydride abstraction. 11
C.7 (a) Tetraborate (B_4O_7) remains intact. (b) Zr and O sites are more exposed. Borate cluster is distorted. Borate shifts downward, forming new Zr-O coordination. 12

D.1 Colouring scheme used in the presentation of structures. 13
D.2 Interaction of lewis acid with Tepo,Pyridine,CO 13
D.3 Interaction of lewis acid with Tepo,Pyridine,CO 14
D.4 Interaction of lewis acid with Tepo,Pyridine,CO 14
D.5 Interaction of lewis acid with Tepo,Pyridine,CO 15
D.6 Interaction of lewis acid with Tepo,Pyridine,CO 15

E.1 Example of using consensus for literature search. 16
E.2 Grammarly interface showing grammar and clarity suggestions. 17
E.3 Exmaple of using Chatgpt to simplify and explain scientific concepts. 17

Abbreviations

PP	PolyPropylene
OECD	Organisation for Economic Cooperation and Development
PE	PolyEthylene
MEP	Minimum Energy Path
FCC	Fluid Catalytic Cracking
DFT	Density Functional Theory
i-PP	Isotactic PolyPropylene
TEPO	Triethylphosphine Oxide
CO	Carbon monoxide
NEB	Nudged Elastic Band
SZO	Sulfated Zirconia
BO	Born-Oppenheimer
XC	Exchange-Correlation
LDA	Local Density Approximation
GGA	Generalized Gradient Approximation
PW91	Perdew–Wang 91
PBE	Perdew-Burke-Ernzerhof
BZ	Brillouin Zone
PAW	Projector Augmented Wave
PBCs	Periodic Boundary Conditions
PES	Potential Energy Surface
IR	Infrared
VASP	Vienna Ab initio Simulation Package
HPC	High Performance Computing
SCF	Self-Consistent Field
RMM-DIIS	Residual Minimization Method with Direct Inversion in the Iterative Subspace
CG	Conjugate-Gradient

Abstract

The global plastic waste issue demands recycling technology development beyond the conventional ones, which is limited by contamination, polymer degradation, and energy inefficiency. The thesis describes the potential of main-group-based acid species supported on a zirconia as a catalyst for chemical upcycling of polypropylene (PP), one of the most widely used plastic but difficult to recycle. Inspired by previous study on sulfated zirconia (SZO), which abstract the hydride via its Lewis acidic site, this work explores whether the same activity can be achieved with phosphoric acid, tetraboric acid, boric acid, fluorosulfuric acid, triflic acid, and bistriflimide. Density Functional Theory (DFT) was used to determine adsorption energies, surface saturation effects, Lewis acidity (via probe molecules), and hydride abstraction barriers using Nudged Elastic Band (NEB) analysis. Fluorosulfuric acid and triflic acid were found to activate polyolefins, demonstrating their potential for catalytic upcycling. Also, fluorosulfuric and triflic acid were found to have comparable energy barriers to SZO; however no system studied surpassed SZO in terms of Lewis acidity or overall reactivity.

1

Introduction

Plastics revolutionized the modern world entirely due to their durability, elasticity, and affordability. The use of plastics caused a global environmental problem and and potential danger to the public health [1–3]. Mechanical and chemical recycling are inefficient because of contamination, mixed polymer waste, and degradation of materials, which hinders plastic waste recyclability [4]. This problem requires more effective and more sustainable upcycling technologies. Polypropylene (PP), one of the most widely used plastics, is among the most difficult plastics to mechanically recycle due to chemical additives, stabilizers, and pigments [5]. Classical end-of-life operations are limited, and for this reason, there has been increasing interest regarding upcycling by using heterogeneous catalysis in breaking plastic waste into fuels and chemicals.

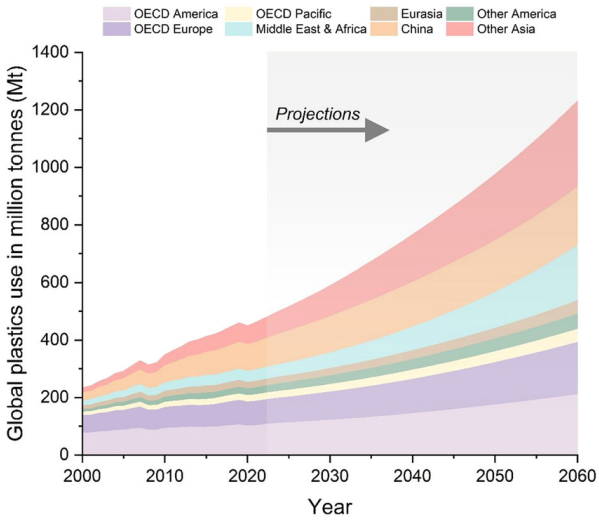

Figure 1.1: Global plastic production: According to Organisation for Economic Cooperation and Development (OECD) projections, the figure shows the expected exponential growth in plastic production over the next forty years [6].

1.1. Limitations of Conventional Plastic Disposal and Recycling

Existing plastic waste recycling have significant limitations. Landfilling requires land and has the potential to lead to serious environmental pollution risks [7]. Incineration produces energy from plastic waste but is a source of greenhouse gases and harmful emissions [8]. Recycling technologies were developed to reduce the use of these practices.

1.1.1. Mechanical Recycling

Mechanical recycling processes plastic waste to create new materials or products but it does not alter its original chemical composition. [9]. However, contamination, polymer degradation, and recycling of mixed plastics make mechanical recycling challenges continue in the present world [10].Compared to recycling plastics

into their monomers, mechanical recycling does not break the polymer backbone. Impurities such as adhesives,mixed plastics, and dyes have the effect of decreasing the mechanical properties of the recycled plastics. The mechanical recycling process operations convert plastics into flakes, powder, or pellets. Since mechanical recycling cannot handle mixed plastic waste, separation technologies such as density separaiton are employed. At the next stage, plastics are formed into new products by various resin molding processes[11]. Plastics are prone to thermo-mechanical degradation through multiple processing cycles. Due to the heat and shear involved in extrusion and molding, chain scission and molecular weight loss occur, which degrades mechanical properties such as impact resistance and tensile strength[11]. In addition, PE contamination is also present in common mixed plastic waste, which is a serious issue. Since PP and PE are immiscible, recycled blends possess inferior mechanical characteristics [12]. The addition of stabilizers and compatibilizers during reprocessing can help counteract such immiscibility, but it increases the complexity and cost of recycling [11].

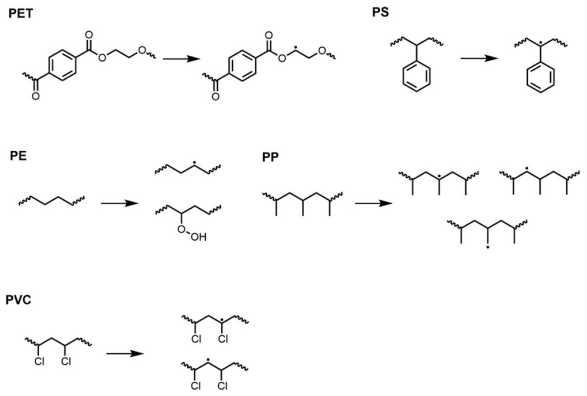

Figure 1.2: Radical formation during the mechanical recycling of common plastics. Mechanical stress and heat generate radicals along polymer chains, such as in PET, PS, PE, PP, and PVC. These radicals may undergo hydrogen abstraction followed by β-scission, leading to chain cleavage [13].

1.1.2. Chemical Recycling

Chemical recycling breaks down plastic waste into its basic molecular components, enabling the creation of polymers with properties equivalent to virgin materials [14]. Unlike mechanical recycling, chemical recycling restores plastics to their monomers or oligomers. Chemical recycling effectively handles contaminated, mixed, or degraded plastics to transform the waste into high-quality materials instead of lower-grade material [15]. Impurities like dyes, plasticizers, and food residues should be removed before processing since they would affect depolymerization reactions and the quality of the end product [16]. Chemical recycling is generally divided into two categories: catalytic upcycling and monomer recovery. Generally, polymers are broken into their original monomers, thereby developing a closed-loop recycling which they can be repolymerized to something with properties similar to virgin plastics. Contrarily, catalytic upcycling a newer technique is not meant to recreate the same polymers, but to turn plastics waste into chemical feedstocks. Polyolefins like PE and PP, which are hard to break down into their monomers can be selectively cleaved. Catalytic upcycling, in many cases, relies on targeted bond-breaking mechanisms like β-scission that produce functionalized chemical intermediates that serve as building blocks for advanced polymer materials, synthetic lubricants, or specialty chemicals [17].

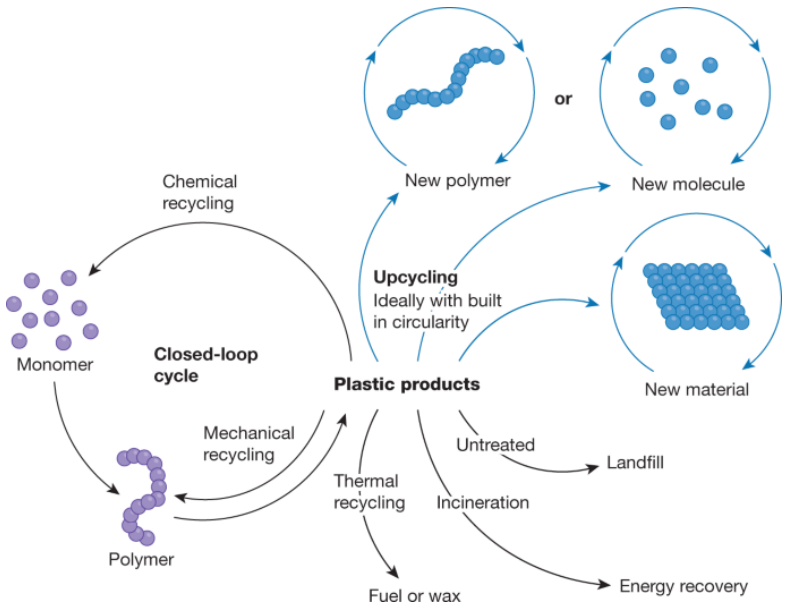

Figure 1.3: Overview of chemical recycling pathways, including monomer recovery and catalytic upcycling. Catalytic upcycling enables selective polymer breakdown into high-value chemical intermediates rather than direct monomer regeneration [18].

1.1.3. Comparison of Mechanical and Chemical Recycling

Table 1.1: Comparison of Mechanical and Chemical Recycling

Aspect	**Mechanical Recycling**	**Chemical Recycling**
Energy Consumption	Requires less energy since it physically alters polymers [19].	Consumes more energy compared to mechanical recycling [20].
Cost	Costs less due to efficient processes and well-established infrastructure [11].	High costs due to large energy demand [21].
Plastic Compatibility	Requires clean and sorted plastics [22].	Can recycle mixed, dirty, and degraded plastics [23].
Material Quality	Repeated recycling can degrade plastic quality [10].	Converts polymers into high-value chemical feedstocks or monomers for closed-loop recycling [13].
Scalability	Widely used on an industrial scale [11].	Limited by high costs and energy demands [24].

Because of these limitations of existing recycling methods, heterogeneous catalysis has become an important approach to improve the sustainability and efficiency of transforming plastic waste into valuable products.

1.2. Chemical Upcycling Pathways and Catalytic Approaches

Chemical recycling processes involve hydrogenolysis and pyrolysis. The processes vary based on product selectivity, operating conditions, and catalyst selection. Catalytic systems from heterogeneous catalysts to homogeneous transition-metal complexes and enzymes have been studied. While high reactivity has been shown using homogeneous and enzymatic systems, their susceptibility to contaminants, recovery , and recycling challenges limit their industrial use [25, 26]. On the other hand, heterogeneous catalysts, which are separable easily, are the most viable catalyst type for industrial plastics upcycling [27].

1.2.1. Pyrolysis

Pyrolysis is among the recycling processes where polymers are transformed into liquid oil, solid residues, and gases under high temperatures [28]. Pyrolysis takes place at varying temperatures of 300–900 °C [29].

Pyrolysis consists of three types, which depend on the operating conditions [29]. The first type is slow heating, where the main product is char, and this type of pyrolysis takes place without oxygen. The second type is fast pyrolysis, where heating is done under controlled temperatures up to 500 °C; additionally, bio-oil is the main product. Flash pyrolysis is characterized by extremely rapid heating and short residence times. The major products obtained from this process are bio-oil and various gases. Fast pyrolysis is preferable in the industry due to its high yield of oil. The pyrolytic degradation of plastics generally involves three key reaction types: chain scission, reactions involving side groups, and recombination[30]. The general equation for the reactions that occur in pyrolysis is given by [31]:

$$C_xH_yO_z + Q \rightarrow Liquid + Gas + Char + H_2O \tag{1.1}$$

Most common plastic waste are PP and polyethylene (PE); therefore, the pyrolysis temperature is set based on their degradation temperatures to get the most liquid products as seen in figure 1.4. 450 °C to 500 °C is the temperature range where degradation occurs[32]. Gas products will be dominant above degradation temperature, and solid residue will be the major product below it.

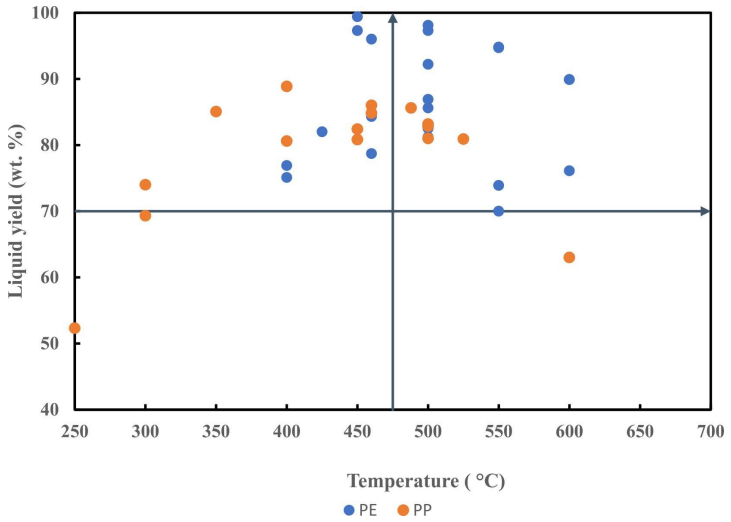

Figure 1.4: Effect of pyrolysis temperature on liquid yield (wt.%) PE and PP [32].

One of the challenges in pyrolysis is that high temperatures are typically required for pyrolysis, leading to significant energy demands[33]. Another challenge is that pyrolysis oil products have unwanted properties, such as high aromatics, waxes, and char content. Pyrolysis oil upgradation therefore typically includes purification to remove impurities, distillation, and fuel blending [33, 34].

1.2.2. Catalytic Pyrolysis

To improve the performance of pyrolysis, catalytic pyrolysis has been introduced to address the limitations of conventional pyrolysis. The benefit of using catalysts is lowering the operating temperature of pyrolysis. In addition, the catalysts can modify the energy barrier for the reactions or alter the minimum energy path (MEP). Catalysts used in pyrolysis are heterogenous due to the fact that they can be separated easily from the products[35]. Catalytic pyrolysis produces a higher yield of gaseous products than liquid products.[36]. Catalytic pyrolysis is classified as in-situ and ex-situ processes. In the in-situ process, catalyst and feedstock are blended in a homogeneous reactor, wherein both catalytic upgrading and pyrolysis occur. In the ex-situ process, the catalyst is used in another reactor, where it upgrades the pyrolysis vapors[37]. Catalytic pyrolysis is divided into in-situ and ex-situ processes. In the in-situ process, the feedstock and catalyst are blended together in a single reactor such that pyrolysis and catalytic upgrading occur. In the ex-situ process, the catalyst exists within another reactor where it upgrades pyrolysis vapors[37]. In the in-situ process, catalyst is mixed with solid residues. In the ex-situ process, it is not mixed with plastic feedstock, and recovery is easy[32]. Catalysts used in pyrolysis are mostly zeolites[38, 39].

Figure 1.5: Simplified mechanism of zeolite-catalyzed hydrocarbon cracking. The catalyst activates the alkane by protonation or hydride removal, forming a reactive carbenium ion. This ion undergoes β-scission, breaking carbon-carbon bonds to form smaller molecules. The cycle continues, producing lighter products through repeated cracking steps[40].

1.2.3. Hydrogenolysis

Hydrogenolysis is a reaction in which polymer chains are broken into low molecular weight hydrocarbons via transition-metal catalyzed cleavage of carbon-carbon bonds in the presence of hydrogen[41]. Hydrogenolysis has been suggested as a potential future prospect for upcycling plastic waste but it is still at laboratory research stage[42, 43]. Hydrogenolysis, as opposed to pyrolysis, takes place under comparatively milder conditions. The reaction parameters can be adjusted to suit specific polyolefin feedstock and can achieve reasonable product selectivity while lowering the energy requirements[44]. Various metal catalysts have been explored for hydrogenolysis reactions, including ruthenium (Ru), iridium (Ir), and copper (Cu)[41]. Ruthenium (Ru) supported on various materials has been extensively studied as a catalytic system, although its effectiveness across different supports remains unclear [45]. One of the research works explored the depolymerization of PP in a relatively mild condition (200–250 °C, 20–50 bar H_2), and it was found that 5 wt% Ru/C nanoparticles achieved over 68% yield of C_5–C_{32} iso-alkanes[42]. Mass transport and poor selectivity to C-C bond cleveage are drawbacks of hydrogenolysis and it can lead to methane (CH_4) formation[42]. Polyolefin hydrogenolysis, as indicated in Figure 1.6, involves polymer adsorption, bond activation, and chain scission. First, the polymer adsorbs on the metal surface (M), where neighboring carbon atoms are dehydrogenated, weakening C–C bond. The polymer is split into two fragments, which are hydrogenated and released as small saturated hydrocarbons. Metal catalyst type and reaction conditions influence selectivity for C–C bond scission, finally determining product distribution. Noble metal based catalysts are used widely in hydrogenolysis; however their limitations such as cost, scarcity and vulnerability to impurities make them not viable option in the long term. Researchers are looking towards more environmentally friendly catalytic systems to overcome these drawbacks; the trend is shifting towards earth-abundant alternatives.

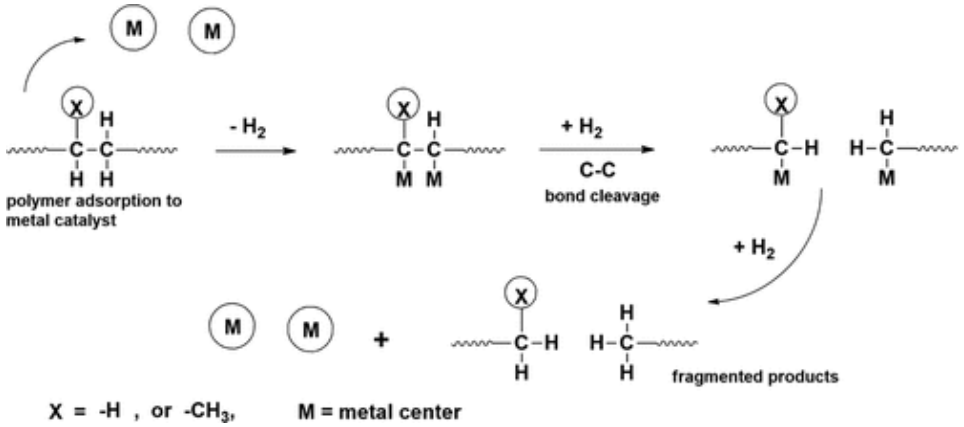

Figure 1.6: General hydrogenolysis mechanism over metal catalysts. Polymer chains adsorb to the metal surface, and undergo dehydrogenation, followed by C–C bond cleavage and rehydrogenation to form shorter saturated hydrocarbons[42].

1.2.4. Catalytic upcycling on sulfated zirconium oxide

Catalytic upcycling of polyolefins is based on activation of inactive C–H and C–C bonds to enable their tranformation to useful chemical feedstocks. Sulfated zirconia (SZO) has been shown to be a potential upcycler of polyolefins due to its active Lewis acid sites that enable hydride abstraction and resulting in β-scission of polymer chains [46]. According to Jammee et al., the catalytic activity of SZO is closely linked to the presence of pyrosulfate groups ($S_2O_7^{2-}$) on the ZrO_2 surface. During C–H bond activation, the pyrosulfate group's S–O–S bond is broken to yield SO_3 intermediate. The highly active intermediate is a Lewis superacid that abstracts a hydride from the polymer to yield a carbocation intermediate. The intermediate is responsible for causing β-scission, in which C–C bonds are selectively cleaved to fragment the polymer into short hydrocarbon chains. Also Jammee et al. found that SZO SO_3 intermediate significantly lowers the energy barrier for hydride abstraction.

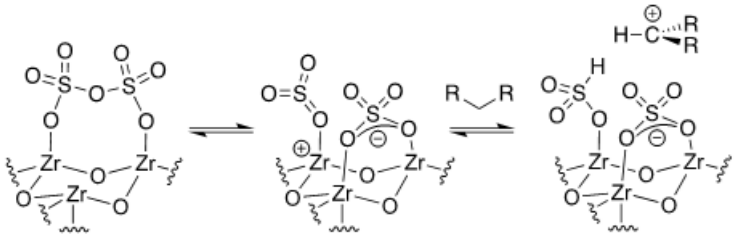

Figure 1.7: C–H bond activation on sulfated ZrO_2, showing pyrosulfate bond cleavage, transient SO_3 formation, and hydride abstraction leading to carbocation generation [46].

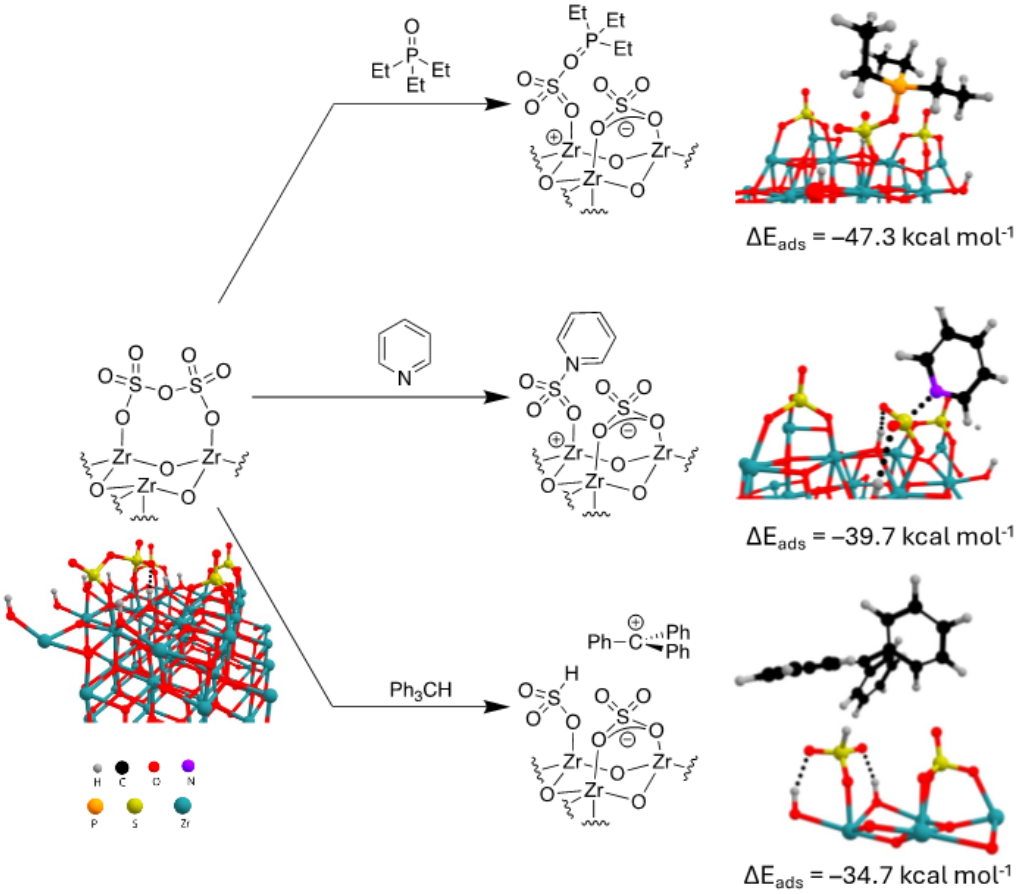

Figure 1.8: Lewis acidity probes used in the work of Jammee et al.

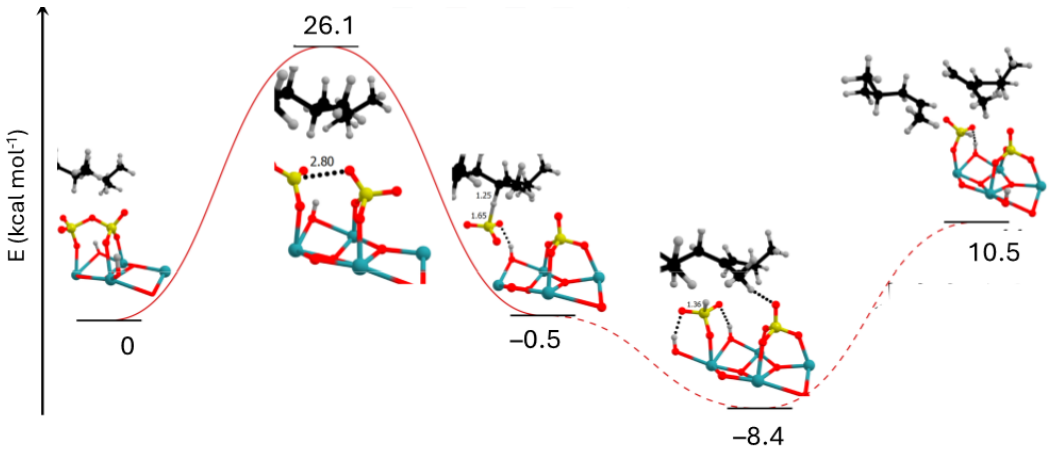

Figure 1.9: Reaction profile for sulfated zirconia (SZO) from the work of Jammee et al.

Inspired by these findings, the acids in figure 1.10 were selected to determine if they can produce active sites on ZrO_2 that can support hydride abstraction similar to SZO. The goal of this work is to determine whether the adsorbed acid in ZrO_2 can follow a similar path and display analogous or even better catalytic properties.

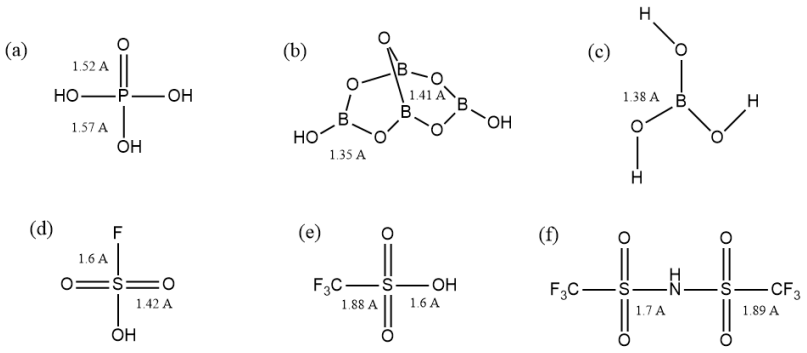

Figure 1.10: (a) H_3PO_4 (Phosphoric acid), (b) $H_2B_4O_7$ (Tetraboric acid), (c) H_3BO_3 (Boric acid), (d) $HFSO_3$ (Fluorosulfuric acid), (e) CF_3SO_3H (Triflic acid), and (f) $(CF_3SO_2)_2NH$ (Bis-triflimide). Bond distances are given in angstroms (Å).

1.3. Computational Approach and Thesis Objectives

Computational chemistry advances, particularly in Density Functional Theory (DFT), have revolutionized catalyst optimization and design. DFT calculations allow the prediction of essential catalytic parameters before experimental validation, providing insight into electronic structure, adsorption energies, and reaction barriers [47, 48]. As aforementioned one new discovery confirmed by both experiment and DFT that SO_3 enables hydride abstraction from polyolefin [46]. The goal of this thesis is computationally examine the catalytic activity of main-group-based supported on the ZrO_2 surface. Acid species used in this research are phosphoric acid, tetraboric acid, boric acid, fluorosulfuric acid, triflic acid, and bistriflimide. The adsorption energies are first examined to determine stability and surface saturation influence. Reaction energy is then investigated through simulation of hydride transfer from a model isotactic polypropylene (i-PP) trimer to the Lewis acid. In addition to this, Lewis acidity is quantified via usage of probe molecules such as Triethylphosphine Oxide (TEPO), carbon monoxide (CO), and pyridine. For a better description of the kinetics of hydride abstraction, calculations are done based on Nudged Elastic Band (NEB) to compute barriers for the systems. Finally, calculation of vibrational frequencies is carried out to confirm the transition state. All these results will finally be towards the identification of the most promising plastic upcycling catalysts based on thermodynamic and kinetic reasonings.

2

Theory

2.1. Density Functional Theory

DFT is a fundamental method for describing the electronic structure of molecules, enabling the calculation of crucial properties. It is widely used in chemistry, physics, and materials science. DFT seeks to solve the Schrödinger equation, which describe the quantum behavior of electrons. The information in this section is based on the books *Density Functional Theory: A Practical Introduction* and *A Chemist's Guide to Density Functional Theory* [49][50]. The time-independent Schrödinger equation is given by:

$$\hat{H}\psi = E\psi \tag{2.1}$$

where $\hat{H}$ is the Hamiltonian operator, ψ is eigen states and has associated eigen values E. The wavefunction ψ contains all the information about the quantum state, while the Hamiltonian describes the total energy, consisting of kinetic and potential energy terms. For simple cases such as hydorgen atom, the Schrödinger equation can be solved exactly. However, for large systems, which contain many interacting electrons and nuclei, solving the full equation directly becomes impossible. The Hamiltonian for many body system is given by:

$$\hat{H} = -\frac{1}{2}\sum_{i=1}^{N}\nabla_i^2 - \frac{1}{2}\sum_{A=1}^{M}\frac{1}{M_A}\nabla_A^2 - \sum_{i=1}^{N}\sum_{A=1}^{M}\frac{Z_A}{r_{iA}} + \sum_{i=1}^{N}\sum_{j>i}^{N}\frac{1}{r_{ij}} + \sum_{A=1}^{M}\sum_{B>A}^{M}\frac{Z_A Z_B}{R_{AB}} \tag{2.2}$$

The first term represents the kinetic energy of electrons, while the second describes the kinetic energy of nuclei. The third term accounts for the electron-nucleus interaction, the fourth for electron-electron repulsion, and the final term for nucleus-nucleus repulsion. Important simplification comes from the observation that electrons are much lighter and move much faster than nuclei. This leads to the Born-Oppenheimer (BO) approximation, which assumes that the electron and nuclear motion can be separated. So in Equation 2.2 the second terms is neglected since BO assumed that nuclei motion is constant relative to the electrons. Additionally, the last term in equation 2.2 becomes constant and the equation reduced to electronic Hamiltonian

$$\hat{H}_{\text{elec}} = -\frac{1}{2}\sum_{i=1}^{N}\nabla_i^2 - \sum_{i=1}^{N}\sum_{A=1}^{M}\frac{Z_A}{r_{iA}} + \sum_{i=1}^{N}\sum_{j>i}^{N}\frac{1}{r_{ij}} \tag{2.3}$$

The solution to Schrödinger equation with an electron Hamiltonian is the electronic wave function with eigen values E_{elec} . The electronic wavefunction depend only on the spatial coordinates

$$\hat{H}_{\text{elec}}\Psi_{\text{elec}}(\boldsymbol{r}_1,\ldots,\boldsymbol{r}_N) = E_{\text{elec}}\Psi_{\text{elec}}(\boldsymbol{r}_1,\ldots,\boldsymbol{r}_N) \tag{2.4}$$

Ψ_{elec} is a function of electron position $\boldsymbol{r}_i$ only. It is not easy to determine Ψ_{elec} to obtain the ground state energy E_{elec} because of the electrons interaction. For any given set of coordinates, it is impossible to observe the wavefunction directly. The measurable quantity is the probability that the N electrons are at a specific set of coordinates, $r_1,\ldots,r_N$. This probability is given by:

$$|\Psi(r_1,\ldots,r_N)|^2 = \Psi^*(r_1,\ldots,r_N)\Psi(r_1,\ldots,r_N) \tag{2.5}$$

$$|\Psi(\boldsymbol{r}_1,\ldots,\boldsymbol{r}_N)|^2 = \Psi^*(\boldsymbol{r}_1,\ldots,\boldsymbol{r}_N)\Psi(\boldsymbol{r}_1,\ldots,\boldsymbol{r}_N) \tag{2.6}$$

Equation 2.6 can be approximated using the Hartree product because it allows to treat a complex many-electron wavefunction as a product of single-electron functions

$$\Psi = \psi_1(\mathbf{r})\psi_2(\mathbf{r})\ldots\psi_N(\mathbf{r}) \tag{2.7}$$

The electron density at a particular position in space represents the probability of finding an electron at that location. It is determined by summing over all the probabilities that an electron occupies at a given position, as described by the individual wavefunctions $\Psi(\boldsymbol{r})$. The factor two before the summation in Equation 2.8 accounts for the electron spin, following the Pauli exclusion principle. Electron density depends only on spatial coordinates, it is a function of three coordinates.

$$n(\boldsymbol{r}) = 2\sum_i \psi_i^*(\boldsymbol{r})\psi_i(\boldsymbol{r}) \tag{2.8}$$

DFT is fundamentally based on electron density, with its theoretical foundation established by Kohn and Hohenberg through two key theorems[51]. The first theorem states that "the ground-state energy E, as derived from Schrödinger's equation, is uniquely determined by the electron density $n(\boldsymbol{r})$". According to the second theorem, "the correct electron density is the one that minimizes the total energy functional, corresponding to the exact solution of the Schrödinger equation". The functionals described by Kohn and Hohenberg is written in terms of single electron wavefunctions.

$$E\left[\{\psi_i\}\right] = E_{\text{known}}\left[\{\psi_i\}\right] + E_{\text{XC}}\left[\{\psi_i\}\right] \tag{2.9}$$

The first term $E_{\text{known}}[\{\psi_i\}]$ is composed of the electron kinetic energies, the Coulomb interactions between the electrons and the nuclei, the Coulomb interactions between pairs of electrons, and the Coulomb interactions between pairs of nuclei. The second term in Equation 2.9 hold other effects that are not included in $E_{\text{known}}[\{\psi_i\}]$. However, Kohn and Hohenberg did not provide method to find the minimum energy in the functional. Kohn and Sham demonstrated that determining the electron density requires solving a set of equations, each corresponding to a single electron.

$$\left[\frac{1}{2}\nabla^2 + V(\vec{r}) + V_H(\vec{r}) + V_{XC}(\vec{r})\right]\psi_i(\vec{r}) = \varepsilon_i\psi_i(\vec{r}) \tag{2.10}$$

The term $V(\vec{r})$ represents the external potential, which arises from the interaction between electrons and atomic nuclei. The Hartree potential, $V_H(\vec{r})$, accounts for the repulsion between electrons. The exchange-correlation (XC) potential, $V_{XC}(\vec{r})$, incorporates quantum mechanical effects. The Kohn and Sham equation can be solved in iterative way as seen in Figure 3.2.

2.1.1. Exchange-Correlation Functional

In Equation 2.9, the term $E_{\text{XC}}\left[\{\psi_i\}\right]$ is not known exactly, except for a uniform electron gas where the electron density remains constant in space. Therefore, approximations are necessary. The simplest approximation is the Local Density Approximation (LDA), where the XC potential at a given position is assumed to be the same as that of a uniform electron gas at the same density. This approach represents the first rung of Jacob's ladder in Figure 2.1

$$V_{\text{XC}}(\boldsymbol{r}) = V_{\text{XC}}^{\text{electron gas}}[n(\boldsymbol{r})] \tag{2.11}$$

A more advanced approximation is the Generalized Gradient Approximation (GGA), which improves upon LDA by incorporating spatial variations in the electron density.

$$V_{\text{XC}}^{\text{GGA}}(\boldsymbol{r}) = V_{\text{XC}}[n(\boldsymbol{r}), \nabla n(\boldsymbol{r})] \tag{2.12}$$

Common functionals used within GGA include the Perdew–Wang 91 (PW91) and Perdew–Burke–Ernzerhof (PBE) functionals. In this work, the PBE functional is chosen due to its widespread use in heterogeneous catalysis and its ability to provide accurate results at a relatively low computational cost [52]. As one ascends Jacob's ladder, more sophisticated functionals offer greater accuracy but also demand significantly higher computational resources.

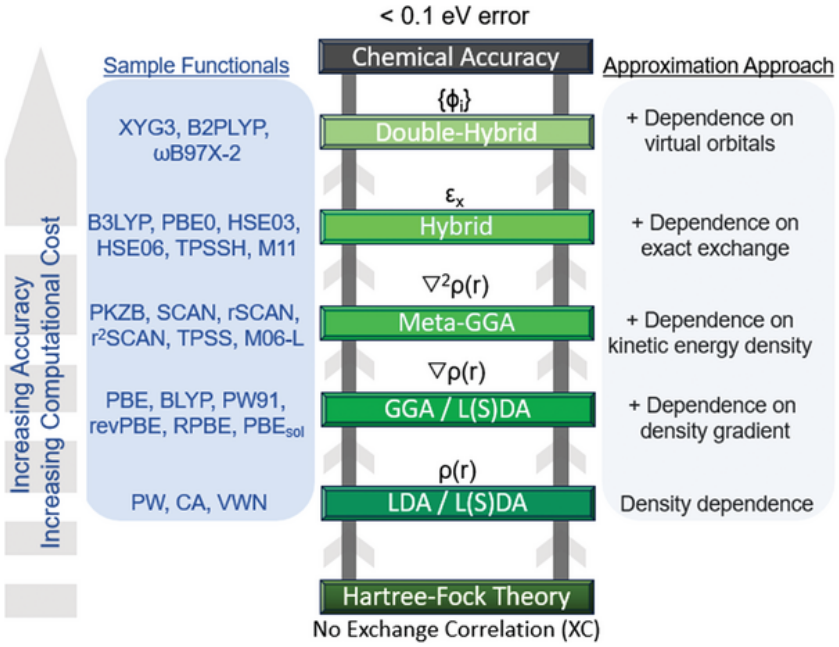

Figure 2.1: Jacob's Ladder of DFT functionals, illustrating the hierarchy from LDA to hybrid functionals [53].

2.1.2. DFT+U: Addressing the Limitations of Standard DFT

Functionals, like LDA and GGA, often over-delocalize electrons due to their inability to accurately describe strong electron-electron interactions in localized orbitals. The DFT+U method introduces an additional Hubbard correction that accounts for on-site Coulomb interactions, improving the localized electronic states, particularly in d and f orbitals. The Hubbard parameter, U, defines the strength of the on-site Coulomb repulsion and is typically determined through either first-principles calculations or semi-empirically. Improvement in DFT+U implementations is the use of a rotationally invariant formulation, which ensures that the correction remains independent of the choice of atomic orbital basis [54].

2.1.3. DFT-D Method

Dispersion interactions, also known as van der Waals forces. Nonpolar molecules lack permanent dipole moments, temporary electron density fluctuations may induce transient dipoles. These transient dipoles cause a dipole in the neighboring atoms, generating an attractive interaction. The dispersion interaction between two spherically symmetric atoms at large separations follows an inverse sixth-power dependence on the interatomic distance:

$$V_{\text{dispersion}} = -\frac{C}{r^6}, \tag{2.13}$$

where C is a system-dependent constant. Most conventional DFT functionals struggle to handle dispersion interactions properly. To counteract this, the DFT-D approach was created.

$$E_{\text{DFT-D}} = E_{\text{DFT}} - S\sum_{i<j}\frac{C_{ij}}{r_{ij}^6} f_{\text{damp}}(r_{ij}), \tag{2.14}$$

where r_{ij} is the distance between atoms i and j, C_{ij} is a coefficient of dispersion calculated from atoms properties, S is an empirical scaling factor parameter, and $f_{\text{damp}}(r_{ij})$ is a damping factor to prevent divergence at short distances.

2.1.4. K-Point Sampling, Plane Waves, and Pseudopotentials

In extended systems, solving the Schrödinger equation in real space is computationally expensive. It is more convenient to work in reciprocal space using Bloch's theorem, which states that the electronic wavefunctions in a periodic system can be expressed as

$$\psi_{nk}(\mathbf{r}) = e^{i\mathbf{k}\cdot\mathbf{r}} u_{nk}(\mathbf{r}) \tag{2.15}$$

where $u_{nk}(\mathbf{r})$ has the same periodicity as the system and $e^{i\mathbf{k}\cdot\mathbf{r}}$ is a plane wave. The set of unique $\mathbf{k}$-points forms the Brillouin Zone (BZ), which is the fundamental region for calculations. Since a full integral over the BZ is computationally costly, a discrete k-point mesh is used to approximate the integral, with the Monkhorst-Pack scheme providing an efficient method for generating a uniform grid of k-points[55]. Metallic systems, due to their discontinuous Fermi surface, require denser k-point grids compared to semiconductors and insulators, and smearing techniques such as Gaussian smearing commonly used to handle these discontinuities. Electronic wavefunctions are expanded in a plane-wave basis since plane waves are more convenient to solve in reciprocal space than in real space, expressed as

$$\psi_k(\mathbf{r}) = \sum_{\mathbf{G}} C_{\mathbf{G},k} e^{i(\mathbf{k}+\mathbf{G})\cdot\mathbf{r}}, \tag{2.16}$$

where $\mathbf{G}$ are reciprocal lattice vectors. Because an infinite number of plane waves would be required for an exact representation, the expansion is truncated using a cutoff energy, given by

$$E_{\text{cut}} = \frac{\hbar^2 |\mathbf{k}+\mathbf{G}|^2}{2m}, \tag{2.17}$$

where a higher cutoff energy increases accuracy but also leads to higher computational costs. Pseudopotentials simplify the calculations by replacing the electron density of core electrons with a smoothed effective potential. Since chemical bonding and other material properties are influenced by valence (outer shell) electrons, core electrons play a minimal role in these interactions. This allows for the use of pseudopotentials to approximate the effect of core electrons without calculating their wavefunctions. This is called frozen core approximation and a common method for achieving this is Projector Augmented Wave (PAW). DFT calculations are typically performed in a unit cell or supercell, which is periodically repeated. This is accomplished through the utilization of Periodic Boundary Conditions (PBCs), causing each unit cell to interact with its periodic images, simulating an infinite system without high computational cost.

2.1.5. Potential Energy Surface

The information in the subsection is based on *Computational Chemistry:Introduction to the Theory and Applications of Molecular and Quantum Mechanics* [56]. The Potential Energy Surface (PES) describes how the total energy of a molecular system varies as a function of the nuclear coordinates. By evaluating the energies for different positions and connecting them, a continuous surface is generated. PES provides insight into reaction intermediates, and transition states along a reaction pathway. Geometry optimization on the PES involves moving atomic positions in the direction of lower energy until a local minimum is reached. When a system of atoms is in a state of equilibrium, there are no net forces acting on any of them. This condition corresponds to a point on the PES where the energy is not changing with respect to the atomic positions, meaning its first derivative is zero.

$$\mathbf{F}(\mathbf{R}) = -\frac{\partial E(\mathbf{R})}{\partial \mathbf{R}} \tag{2.18}$$

However, this condition alone cannot distinguish between a local minimum (stable structure) and a local maximum (transition state). Therefore, the second derivative (curvature) is used: a positive second derivative indicates a minimum, while a negative one indicates a maximum. The 3D structure of PES can be seen in figure 2.3. Saddle points correspond to transition states structures connecting reactants to products via the lowest-energy path. This trajectory is called MEP, and it connects the reactants to products through the transition state.

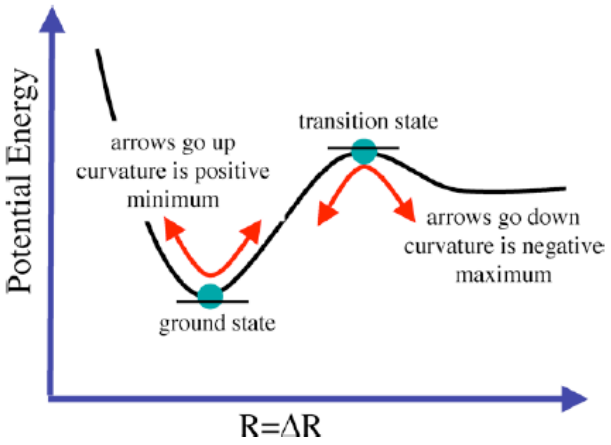

Figure 2.2: PES showing ground state (minimum) and transition state (maximum) [57].

Once a potential transition state is located via NEB it must be verified. This is achieved by performing a vibrational frequency analysis. The vibrational modes, also known as normal modes, represent the characteristic atomic motions of the molecule in response to small displacements. In each mode, all atoms move periodically and in phase. For a nonlinear molecule with N atoms, the number of independent vibrational motions is $3N-6$. In contrast, a linear molecule has $3N-5$ modes. These vibrational frequencies are determined by diagonalizing the Hessian matrix, which contains second derivatives of the energy with respect to atomic displacements. Each eigenvalue corresponds to a vibrational frequency, and each eigenvector indicates the atomic motion involved. A larger force constant corresponds to a stiffer, higher-frequency vibrational mode. For stable structures (minima), all vibrational frequencies are real and positive, indicating that displacements in any direction result in a restoring force. However, a true transition state exhibits one and only one imaginary frequency (corresponding to a negative force constant). This specific vibrational mode aligns with the reaction coordinate and moves the system from reactants to products without a restoring force, confirming the presence of a saddle point on the PES. A conceptual form of the Hessian matrix for a simple 2-atom system (6 degrees of freedom) is:

$$\mathbf{H} = \begin{bmatrix} \frac{\partial^2 E}{\partial x_1^2} & \cdots & \frac{\partial^2 E}{\partial x_1 \partial z_2} \\ \vdots & \ddots & \vdots \\ \frac{\partial^2 E}{\partial z_2 \partial x_1} & \cdots & \frac{\partial^2 E}{\partial z_2^2} \end{bmatrix} \tag{2.19}$$

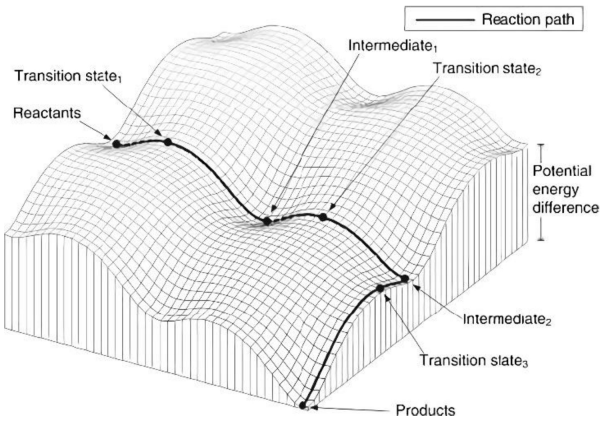

Figure 2.3: Schematic representation of a potential energy surface (PES), showing reactants, products, intermediates, and transition states along the minimum energy path (MEP) [58].

2.2. Adsorption of Acids on ZrO_2 Surface

Condensation reaction takes place when adsorbing acids onto the surface of ZrO_2 leading to removal of water molecule. Dehydration step is crucial for the formation of dimeric species.

2.2.1. Summary of Adsorption & Condensation

Table 2.1: Summary of acid adsorption on ZrO_2. Some acids condense upon adsorption, while others remain unchanged.

Acid	Adsorbed Species	Condensed Form Name
H_3PO_4 (Phosphoric Acid)	$[(OH)O_2P–O–PO_2(OH)]^{2-}$ @ $2H^+$ / ZrO_2	Pyrophosphoric Acid
$H_2B_4O_7$ (Tetraboric Acid)	$B_4O_7{}^{2-}$ @ $2H^+$ / ZrO_2	Tetraboric Acid
H_3BO_3 (Boric Acid)	(HO_2)-B-O-B-(HO_2) @ $2H^+$ / ZrO_2	Diboric Acid
HSO_3F (Fluorosulfuric Acid)	$(O_2FS–O–SO_2F)$ / ZrO_2	Disulfuryl fluoride
CF_3SO_3H (Triflic Acid)	$(F_3CO_3S–O–SO_3CF_3)$ / ZrO_2	Triflic Anhydride
$HC_2F_6NO_4S_2$ (Bistriflimide)	$(F_3C\text{-}SO_2\text{-}N\text{-}SO_2\text{-}CF_3)^{1-}$ @ $1H^+$ / ZrO_2	Bistriflimide

2.3. Adsorption Energy Calculations

To assess the thermodynamic favorability of the adsorbed acid systems, adsorption energy (E_{ads}) was calculated using [59]:

$$E_{ads} = E_{surface+acid} - (E_{surface} + E_{acid(gas)}) \tag{2.20}$$

where the first term is the total energy of surface with the acid adsorbed on it, the second is the total energy of the bare surface, and the third term is the total energy of a single acid in the gas phase. A more negative E_{ads} value indicates stronger adsorption and greater stability of the acid on the surface. The Equation 2.20 also holds for calculating the surface adsorption energy and calculating the interaction energy when measuring lewis acidity.

2.4. Lewis Acidity and Probing Molecules

To characterize the Lewis acidity of adsorbed acids, probe molecules were used to measure interaction energy. TEPO was used as a Lewis base probe allowing acid strength to be assessed through the chemical shift in ^{31}P NMR [60]. CO was chosen as probe due to the fact that its vibration frequency vary and can be analyzed by infrared (IR) spectroscopy, providing information regarding acid site strength [61]. Pyridine was also employed as Lewis acidity probe since it coordinates with acid site by nitrogen lone pair, and the adsorption strength is evaluated by IR spectroscopy or ^{15}N NMR [62]. In this work only adsorption energies were calculated.

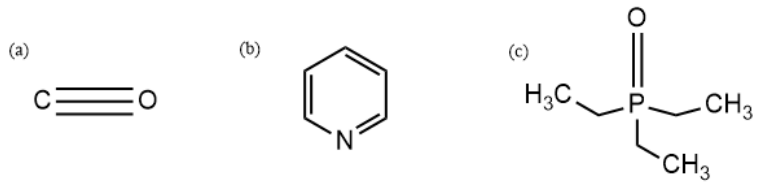

Figure 2.4: Probing molecules used to evaluate interaction energy. (a) CO (b) Pyridine (c) TEPO.

3

Methods

3.1. Computational Setup

DFT calculations were performed using the Vienna Ab initio Simulation Package (VASP) version 5.4.4 [63]. The PBE functional within GGA was used to describe exchange-correlation interactions [64]. A plane-wave energy cutoff of 550 eV. BZ sampling was conducted using a $2 \times 2 \times 1$ Monkhorst-Pack k-point grid centered at Gamma-point (Γ) sampling applied to simplify calculations for large surface models. To accurately account for the localized d-electrons of zirconium, DFT+U was applied. In addition, dispersion interactions were included using the DFT-D correction.

3.1.1. Surface Model

The tetragonal ZrO_2(101) surface was selected for this because of its importance in catalytic applications[65]. The (101) surface has been identified as the most stable facet of tetragonal zirconia, as demonstrated in prior studies and more recently by Jammee et al. [46, 66]. The surface model consists of a 144 atoms, 96 of which are oxygen and 48 zirconium. To simulate bulk-like behavior, the bottom two layers of the slab are held fixed during relaxation while the top layers are allowed to relax freely. In this work, the surface model was taken from Jammee et al. to do this study.

3.1.2. High-Performance Computing: Snellius Supercomputer

All calculations were conducted on the Snellius Supercomputer, the national high-performance computing (HPC) facility of The Netherlands, operated by SURF [67].

3.1.3. VASP Input Files

To perform these calculations, the following VASP input files were required. The POSCAR file follows a structured format to define the atomic configuration for a simulation. As shown in Figure 3.1, the first line contains an optional text description of the system. The second line specifies the scaling factor, which scales the lattice vectors. Lines three to five define the lattice vectors in Cartesian coordinates, specifying the unit cell dimensions. Lines six and seven list the element symbols and the number of atoms for each element. Line eight may optionally include the Selective Dynamics keyword, which allows specific atoms to be constrained during relaxation by using T (True) or F (False) flags. Line nine specifies whether the atomic coordinates are provided in Direct (fractional) or Cartesian format. Line ten and beyond list the atomic positions, where each line contains the (x, y, z) coordinates of the atoms. The KPOINTS file in figure (put figure) A specifies the k-point sampling scheme used to integrate over the BZ. The first line contains an optional description. The second line specifies the number of k-points, and when set to 0, it generate automatic k-points mesh. The third line defines the k-point generation method, in this work we used Monkhorst-Pack . The fourth line provides the k-point grid dimensions 2×2×1 grid is used for sampling. The last line indicates that sampling will start from gamma point. The POTCAR file contains the pseudopotential data for each element. Finally, The INCAR file control the calculation parameters and settings. It specifies key parameters such as the XC, plane-wave cutoff energy (ENCUT), electronic convergence (EDIFF), DFT+U settings and many more.

```
Pyrophosphated_Zirconia
1.0000000000000000
14.6706142425999992    0.0000000000000000    0.0000000000000000
0.0000000000000000   12.8153276442999999    0.0000000000000000
0.0000000000000000    6.2979358163999999   24.0222593051000004
H O P Zr
4 103 2 48
Selective dynamics
Cartesian
7.357055544    8.271325240    8.591843036    T T T
8.881720662    8.073761887    11.421293047    T T T
11.019013152    8.260683544    8.554110183    T T T
```

Figure 3.1: POSCAR file of Pyrophosphated Zirconia, showing lattice vectors, atomic species, atom counts, and cartesian coordinates with selective dynamics.

3.1.4. Geometry Optimization

In VASP, ionic relaxation or geometry optimization is performed iteratively for electronic and ionic steps. The goal is to reach a low-energy, stable structure by varying atoms positions based on forces obtained from the electronic structure. Self-consistent field (SCF) loop, which computes the electronic structure for a given atomic configuration. This involves iteratively solving the Kohn–Sham equations until the electron density converges to a given threshold. Electronic relaxation is performed at every ionic step. VASP employs algorithms such as the Residual Minimization Method with Direct Inversion in the Iterative Subspace (RMM-DIIS) and the conjugate gradient (CG) method for electronic energy minimization. The updated electron density determines the forces that guide the atomic displacements. This process continues iteratively alternating between electronic and ionic steps until the forces on all atoms fall below a predefined threshold. Explanation of the INCAR tags are found in Appendix F

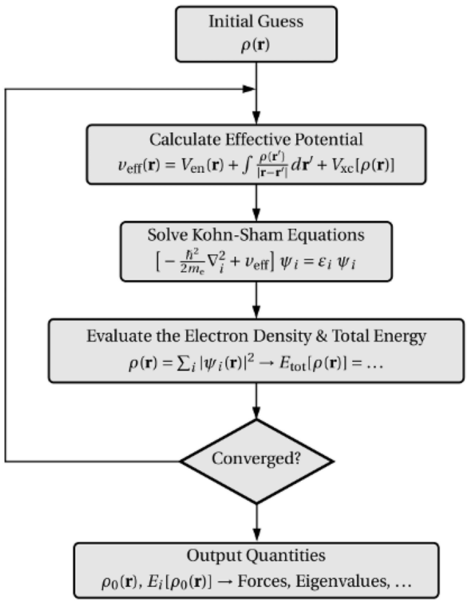

Figure 3.2: Schematic representation of the SCF algorithm used for geometry optimization in VASP[68].

3.1.5. Molecular Visualization and Analysis Using Chemcraft

Chemcraft was utilized throughout the study to construct, visualize and analyze molecular structures[70]. It was particularly useful for building and modifying the POSCAR file by positioning the atoms as seen in Figure 3.1, the positions of the atoms can be extracted from chemcraft for simulations. Additionally, it was used in the analysis of reaction, especially NEB calculations, where it was used to examine transition states.

Table 3.1: DFT Calculation Parameters for the ZrO_2 (101) Surface Model

Parameter	**Description**
Software Package	VASP 5.4.4 [63]
Plane-Wave Energy Cutoff	550 eV
Brillouin Zone Sampling	Monkhorst-Pack 2 × 2 × 1 grid
DFT+U Correction	U = 4 eV applied to Zr d-orbitals [69]
Dispersion Correction	Grimme D3 with Becke–Johnson damping (`IVDW = 12`)
Number of Atoms	144 (96 O, 48 Zr)
Fixed Layers	Bottom two layers fixed, top layers fully relaxed
Electron Spin Configuration	Spin-polarized
Electronic Convergence (EDIFF)	0.1×10^{-4} eV
Ionic Relaxation Convergence (EDIFFG)	0.04 eV/Å

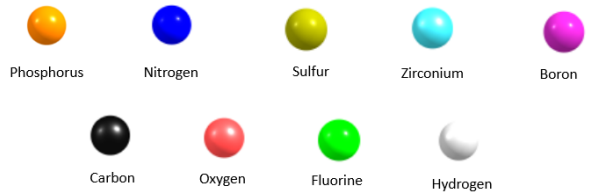

Figure 3.3: Colouring scheme used in the presentation of structures.

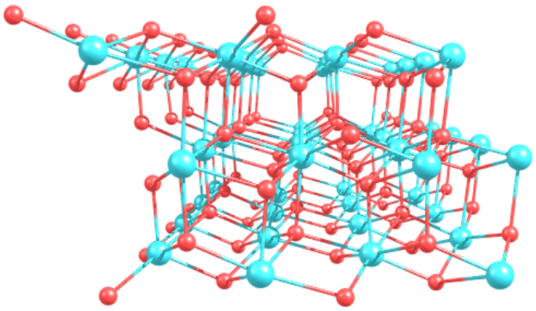

Figure 3.4: Side view of t-ZrO_2 (101) surface.

3.2. Varying Proton Locations

To determine the most stable adsorption configurations, the positions of the protons were varied at different oxygen sites on the surface. Ideally, all inequivalent oxygen atoms should be probed. However, due to large amount of combinations, three to four proton positions were selected for each acid. The variation strategy involved keeping one proton fixed at a particular position and moving the second proton around the acid. The same was done for all acids to make the results comparable. Phosphoric acid is used as an example, and its proton variation is presented in Figure 3.5. The complete set of configurations that were tested for all acids is given in Appendix A. Upon identifying the most stable configuration, the adsorption energy is calculated from Equation 2.20.

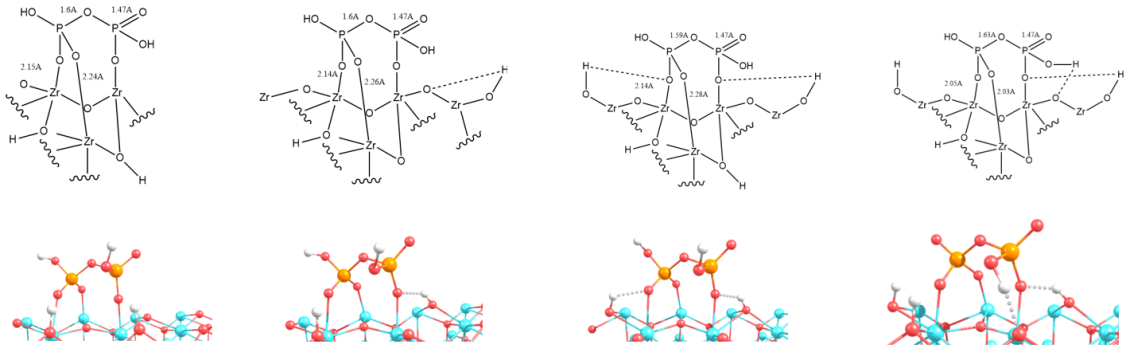

Figure 3.5: Varying proton locations for pyrophosphate adsorbed on the ZrO_2 surface. The top row shows schematic representations with bond lengths (Å), while the bottom row presents corresponding 3D structures.

Table 3.2: Relative energies for different configurations.

Configuration	Relative energy (eV)
a (reference)	0
b	0.40
c	0.92
d	0.75

In relation to Figure 3.5,configuration 1 is the most stable, serving as the reference point with zero relative energy. Configuration 3, on the other hand, is the least stable, as it positions the protons farther from favorable coordination sites. In contrast, Configurations 2 and 4 exhibit intermediate stability, with relative energies of 0.40 eV and 0.75 eV, respectively. These results suggest that proton placement significantly influences the stability of the system, with more favorable coordination leading to lower energy states.

3.3. Surface Saturation

To simulate an actual catalytic high-coverage environment and establish the effect of acid coverage of the surface of ZrO_2, additional acids were adsorbed. This gives the active surface sites complete coverage, simulating conditions relavent in the experimental work. Table 3.3 holds a summary of the saturated surface species.

Table 3.3: Summary of Surface Saturation for Different Acids on ZrO_2.

Acid	Saturated Surface Species	Surface Hydrogens
Phosphoric Acid (H_3PO_4)	${P_2O_7}^{4-} + 3\,{HPO_4}^{2-}$	8
Boric Acid (H_3BO_3)	$H_2B_2O_5 + 3\,{HBO_3}^{2-}$	8
Bistriflimide ($(CF_3SO_2)_2N^-$)	$2\,(CF_3SO_2)_2N^-$	2
Tetraboric Acid ($H_2B_4O_7$)	$2\,H_2B_4O_7$	4
Fluorosulfuric Acid (HSO_3F)	$S_2O_5F_2 + 3\,{SFO_3}^-$	3
Triflic Acid (HCF_3SO_3)	$C_2F_6S_2O_5 + 3\,{CF_3SO_3}^-$	3

The adsorption energy of the fully saturated surface was calculated using Equation 2.20. Phosphoric acid is used as an example to illustrate the surface saturation process in Figure 3.6, while the corresponding saturation configurations for the other acids are provided in Appendix B.

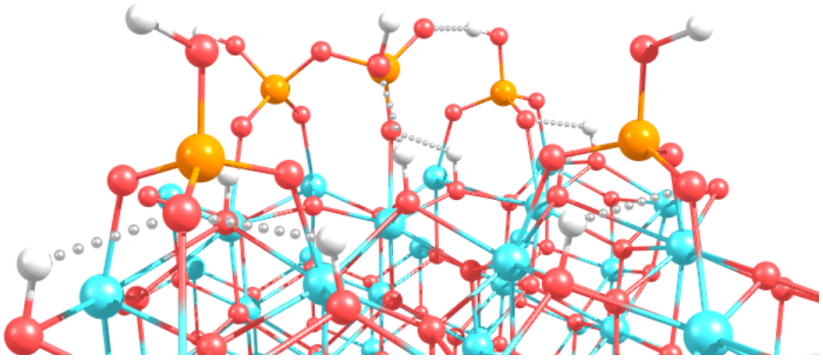

Figure 3.6: Saturation of ZrO_2 surface with phosphoric acid. Three $HPO_4{}^{2-}$ species were added, leading to eight total surface protons.

3.4. Polypropylene activation studies

To assess the reactivity of acid anhydride, we begin by placing the propylene trimer above the anhydride, followed by geometry optimization to obtain the total energy. Next, a C–H bond is broken, and the hydride is transferred to the Lewis acid site, leading to carbocation formation on the trimer. A second geometry optimization is performed to relax the final structure. The reaction energy is given by:

$$\Delta E = E_{\text{final}} - E_{\text{initial}} \tag{3.1}$$

where E_{initial} is the energy when the trimer is on top, and E_{final} is the energy after cleavage, where the hydride is transferred. For illustration, phosphoric acid (H_3PO_4) is used as an example as shown in Figure 3.7. Reactivity figures for all acids are provided in the Appendix C.

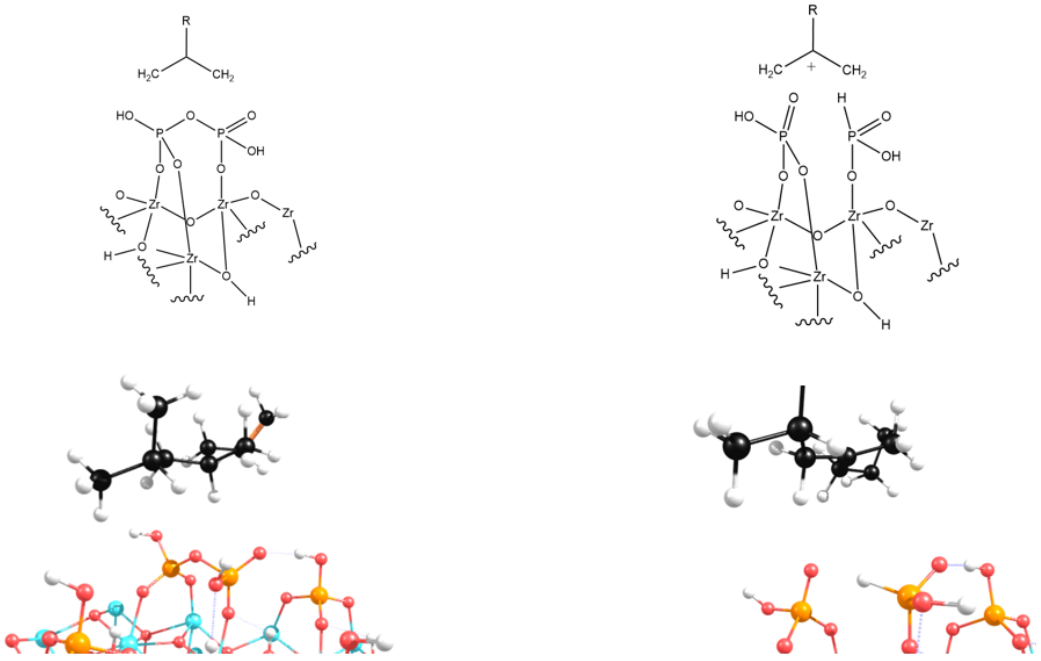

Figure 3.7: (Left) Initial state with trimer on top. (Right) Final state after hydride abstraction.

3.5. Probing Lewis Acids

Probe molecules were introduced after the removal of the trimer and the abstracted hydride. The probes—TEPO, CO, and pyridine were adsorbed onto the exposed Lewis acid sites. Each adsorption configuration was sub-

jected to geometry optimization. The interaction energy (E_{int}) was computed using equation 2.20. Phosphoric acid is used as a representative example, with its interactions with probe molecules shown in Figure 3.8. The figures, including adsorption configurations for all acids, are available in Appendix D.

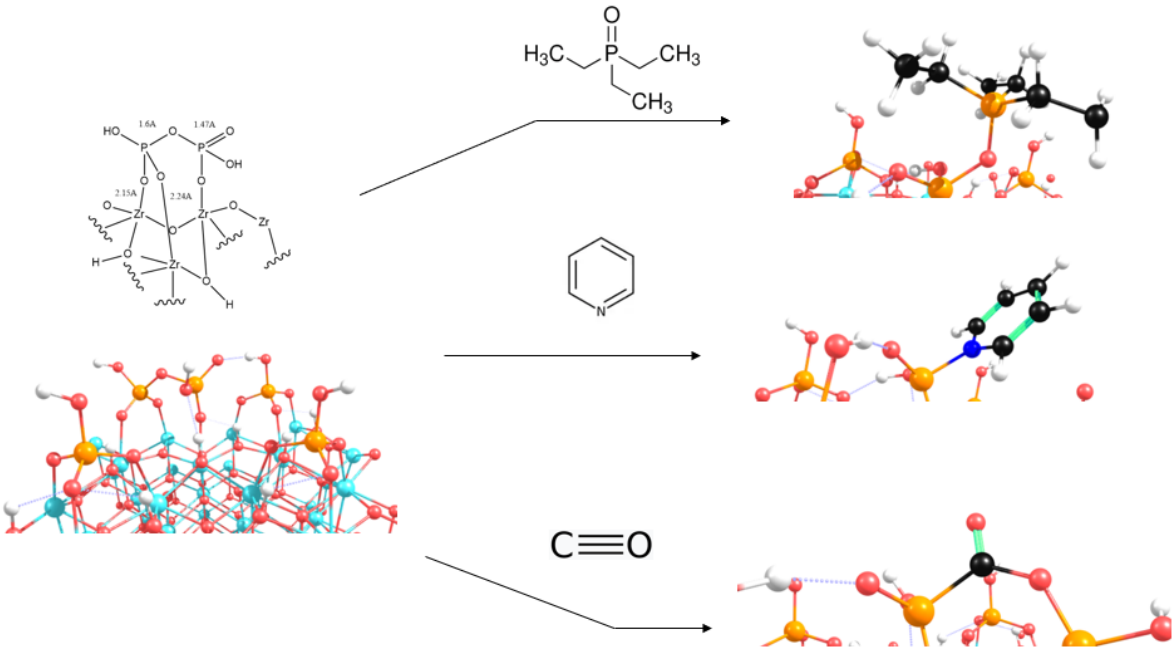

Figure 3.8: Interaction of TEPO, CO, and Pyridine with the Lewis acid site.

3.5.1. Nudged Elastic Band

The NEB approach is used for determining the MEP between reactants and products because the reactant and product are known. It does this by using linear interpolation to create a sequence of intermediate images between the two states. In order to ensure an even distribution along the reaction pathway, these images are optimized simultaneously. Spring forces are added between adjacent images to stop images from collapsing into the reactant or product states [71]. By enhancing the highest-energy image along the reaction coordinate and guaranteeing that it converges precisely to the transition state, the Climbing Image NEB (CI-NEB), as shown in figure 3.10, improves the accuracy of locating transition state [72]. The activation energy ($\Delta E_{activation}$) required for a reaction is determined as:

$$\Delta E_{activation} = E_{TS} - E_{initial} \tag{3.2}$$

where E_{TS} is the energy of the transition state, and $E_{initial}$ represents the energy of the reactant state.

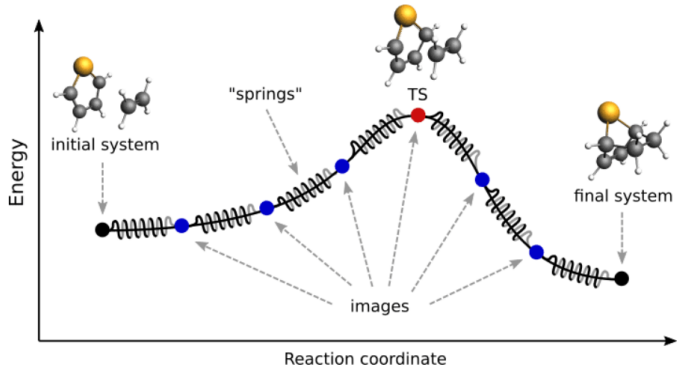

Figure 3.9: Illustration of the NEB method, showing interpolated images along the reaction path and the transition state at the energy maximum. Spring forces maintain a uniform distribution of images along the path [71].

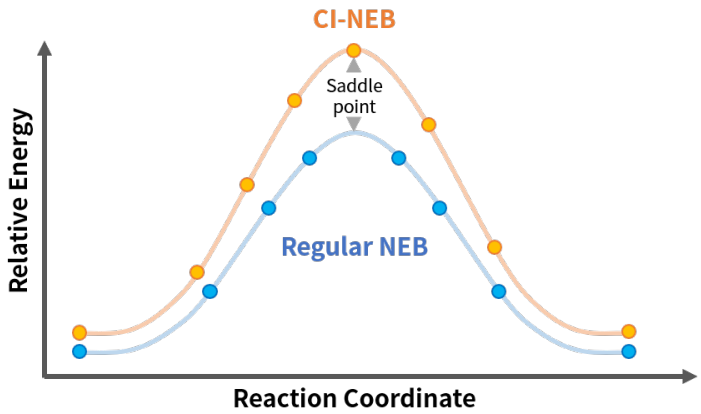

Figure 3.10: Comparison of Regular NEB and CI-NEB, highlighting CI-NEB's improved accuracy in locating the true transition state [73].

4

Results & Discussion

The analysis of the results starts with adsorption energy calculations for the different systems, followed by saturation of the surface to determine its effect on the adsorption energy. Also, Reactivity is calculated by to determine whether the hydride transfer to the lewis acid site is thermodynamically favorable or not. Probe molecules are used to quantify the interaction energies of lewis acids. Finally, NEB calculations are performed to determine the barriers for hydride transfer and locating transition state. After locating the transition state, vibrational calculations are performed to confirm its existence.

4.1. Adsorption Energy of Acid Species

The adsorption energies of six acid molecules on the ZrO_2 surface were computed to assess their interactions with the surface. The results, shown in Table A.4 (Appendix A), highlight a clear distinction between molecules that adsorb favorably and those that do not. Phosphoric acid exhibits the strongest adsorption with an energy of −4.53 eV, followed by boric acid (−2.56 eV), bistriflimide (−2.4 eV), and tetraboric acid (−0.05 eV). These negative values indicate thermodynamically favorable interactions with the surface. In contrast, fluorosulfuric acid and triflic acid show positive adsorption energies (0.26 eV and 0.13 eV, respectively). From a chemical point of view adsorption energies are generally expected to have negative adsorption energies because new surface interactions stabilize the system. The observation of positive energies here suggests that the adsorption is accompanied with condensation and that is energy demanding. This behavior is particularly noticeable for fluorosulfuric acid and triflic acid . These trends are illustrated in Figure 4.1, where positive adsorption energies are marked in red and negative ones in blue.

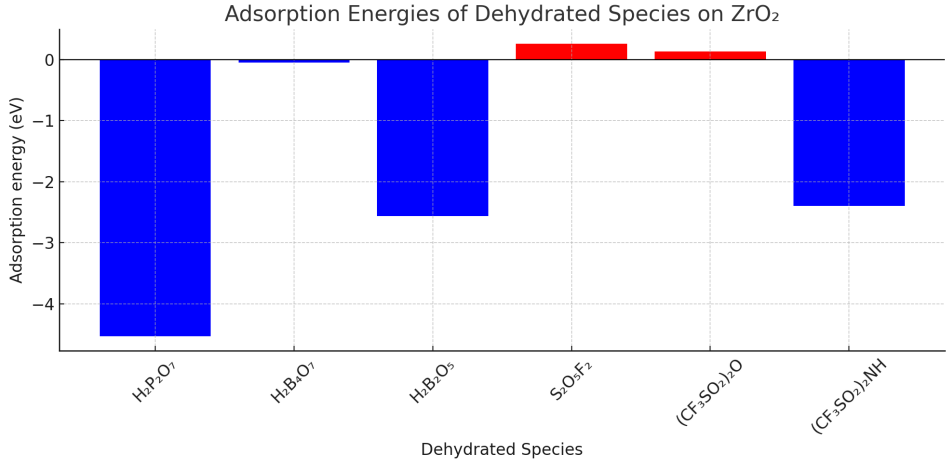

Figure 4.1: Adsorption energies of acid molecules on the ZrO_2 surface.

4.2. Saturation Adsorption Energy

The effect of surface saturation on adsorption strength is illustrated in Figure B.8, which compares the adsorption energies before and after saturation of the surface. The active species and protons on the surface for saturation are summarized in Table 3.3. For the figures related to surface saturation, refer to Appendix B and for the adsorption energies for saturation, are in Table 4.1. As previously discussed in Section 4.1, before saturation, several acids exhibited weak interaction with the surface which are triflic and fluorosulfiric acids, which showed positive adsorption energies. After saturation, however, all species exhibited more negative adsorption energies, indicating enhanced interaction with the surface. This stabilization is attributed to the presence of active sites on the surface and increased proton coverage. Pyrophosphoric acid exhibited the strongest adsorption after saturation (−14.10 eV), while even initially weak adsorbates such as triflic and fluorosulfiric became strongly adsorbed. To further investigate whether there is a correlation between adsorption energies and Lewis acidity, the acidity was evaluated through probe molecules adsorption.

Table 4.1: Adsorption saturation energy per molecule for different compounds.

Molecule	**Dehydration**	**Adsorption energy (eV/molecule)**
H_3PO_4	$ZrO_2 + 5H_3PO_4 \longrightarrow [H_2P_2O_7, 3HPO_4, 8H/ZrO_2] + H_2O$	-2.82
$H_2B_4O_7$	$ZrO_2 + 2H_2B_4O_7 \longrightarrow [2B_4O_7, 4H/ZrO_2]$	-1.70
H_3BO_3	$ZrO_2 + 5H_3BO_3 \longrightarrow [H_2B_2O_5, 8H, 3HBO_3/ZrO_2] + H_2O$	-1.26
$HSFO_3$	$ZrO_2 + 5HSFO_3 \longrightarrow [S_2O_5F_2, 3H, 3SFO_3/ZrO_2] + H_2O$	-1.53
HCF_3SO_3	$ZrO_2 + 5CF_3SO_3H \longrightarrow [(CF_3SO_2)_2, 3H, 3CSF_3O_3/ZrO_2] + H_2O$	-1.1
$(CF_3SO_2)_2NH$	-	-1.53

4.3. Probing Lewis Acidity

As aforementioned to assess the Lewis acidity adsorption of three probe molecules TEPO pyridine, and CO were examined on the anhydride species derived from phosphoric acid, reorganized tetraboric acid,boric acid, fluorosulfuric acid, and triflic anhydride and the figures are in Appendix D. The energies calculated are not only adsorption but bond breaking are involved in this also to form this kind of adducts. For pyrophosphoate, all three probes exhibited weak and unfavorable interactions with positive interaction energies of 0.12 eV with TEPO, 0.14 eV with pyridine, and 0.21 eV with CO, respectively. Despite CO forming a carboxyl species, its interaction remains energetically unfavorable. In contrast, the reorganized tetraboric acid surface shows significantly more favorable interactions: TEPO, pyridine, and CO adsorb with interaction energies of –1.89 eV, –1.60 eV, and –0.81 eV, respectively. For diboric acid favorable interaction occurs upon adsorbing TEPO and CO with interactions of -0.49 and -0.17 eV but in pyridine case the interaction is unfavorable with value of 1.01 eV. Disulfuryl fluoride also shows favorable interactions with values of –1.82 eV for TEPO, –1.42 eV for pyridine, and –0.56 eV for CO, again with carboxyl formation observed. Triflic anhydride follows the same trend, with interaction energies of –1.12 eV, –1.23 eV, and –0.68 eV for TEPO, pyridine, and CO, respectively, and carboxyl formation in the case of CO. These results demonstrate that sulfur based anhydrides introduce stronger Lewis acid sites than phosphates, with reorganized tetraboric acid showing the highest interaction energies across all probes. fluorosulfuric acid and triflic acid show strong interactions with Lewis base probes. This suggests that weakly adsorbed species can still generate highly active Lewis acid sites. Thus, adsorption strength alone does not directly predict Lewis acidity strength.

4.4. Hydride Abstraction: Reaction Energies and Kinetics

The figures for reactivity study are illustrated in Appendix C. Bistriflimide system was excluded from further analysis because the hydride transfer formed an unstable fragment. For boric acid, it was decided to abstract a hydride directly from one of the boron atoms rather than breaking a bond. However, NEB calculations revealed an unstable product and a highly positive reaction energy (4.32 eV), leading to its exclusion from further analysis. A notable observation was made during the hydride transfer step for tetraboric acid: as shown in Figure 4.2, surface reorganization occurs after hydride abstraction. The borate structure becomes distorted, leading to exposed Zr–O surface sites and leading the borate unit in the back to shift downward forming new Zr-O coordination. Adsorption energy and surface adsorption energy were calculated for tetra-

boric reorganized acid, with adsorption and saturation adsorption energies of -2.35 eV and -4.42 eV, respectively. The computed reaction energies for the remaining systems are summarized in Appendix C (Table C.1). Among the evaluated systems, tetraboric acid reorganized, phosphoric acid, and triflic acid exhibit relatively high reaction energies (1.58 eV, 1.13 eV, and 0.97 eV, respectively), indicating that hydride transfer in these systems is not energetically favorable. In contrast, fluorosulfuric acid exhibits a slightly negative reaction energy of -0.13 eV, suggesting a favorable hydride abstraction.

4.4.1. NEB Calculations and Reaction Profiles

NEB calculations were performed to locate the transition states and reaction barriers associated with hydride transfer. For tetraboric reorganized it does not give good reaction profile since the barrier is too small with respect to final state. From the NEB reaction profiles, it was found that for most systems, the product is higher in energy than the reactant, indicating an overall endothermic process. However, for fluorosulfuric acid in Figure 4.3, the final state lies lower in energy than the initial state, consistent with its negative reaction energy. This correspond to reaction energy calculations that supported the thermodynamic favorability of hydride abstraction for fluorosulfuric acid.For phosphoric acid, the activation energy (Ea) from NEB is 2.81 eV. For triflic acid, the barrier is 1.12 eV. For fluorosulfuric acid, the NEB barrier is 0.75 eV. The relatively low activation barrier for fluorosulfuric acid further explains its high reactivity. In contrast, the high barriers for phosphoric acid and triflic acid suggest slower hydride abstraction kinetics, consistent with the less favorable reaction energies observed. For vibrational frequency calculations, it has been found exactly one imaginary frequency for all cases

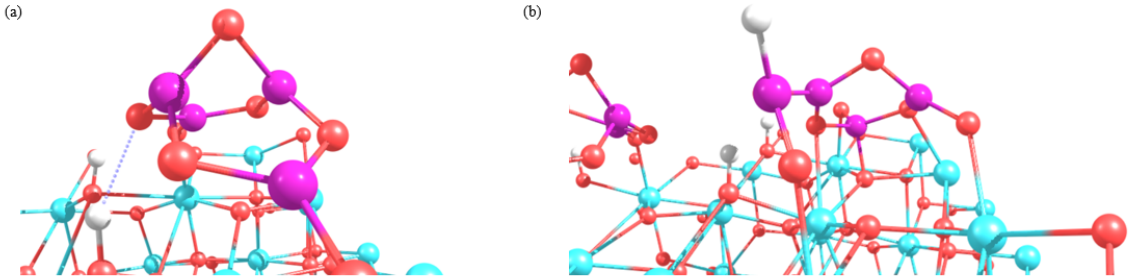

Figure 4.2: (a) Tetraborate (B_4O_7) remains intact. (b) Zr and O sites are more exposed. Borate cluster is distorted. Borate shifts downward, forming new Zr-O coordination.

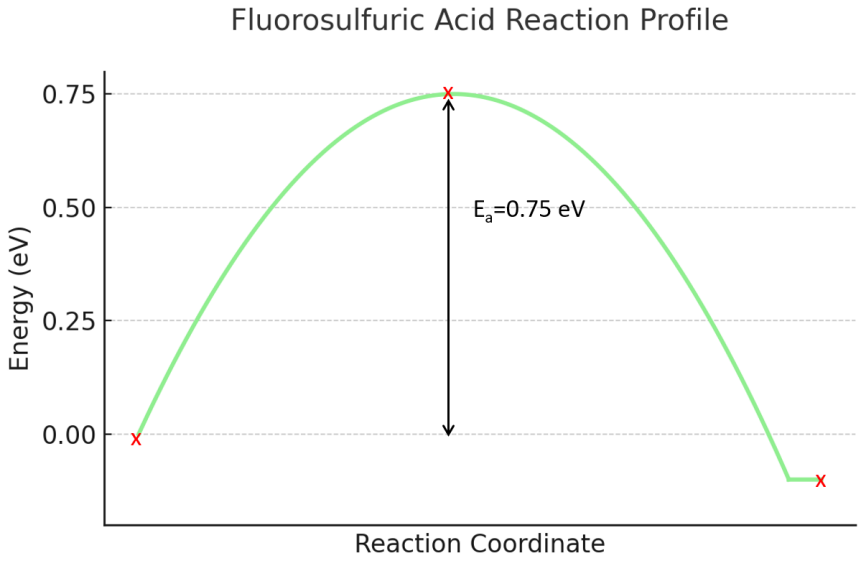

Figure 4.3: Fluorosulfuric acid reaction profile

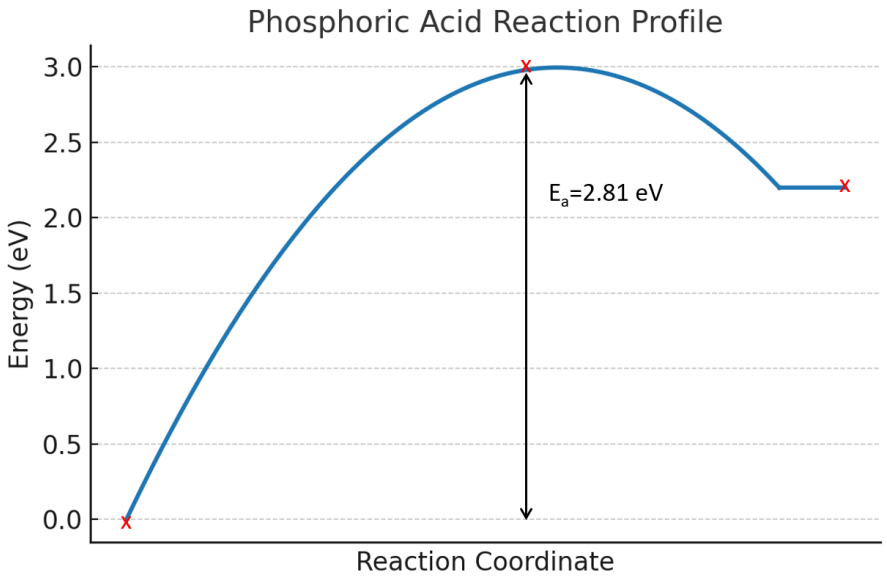

Figure 4.4: Phosphoric acid reaction profile

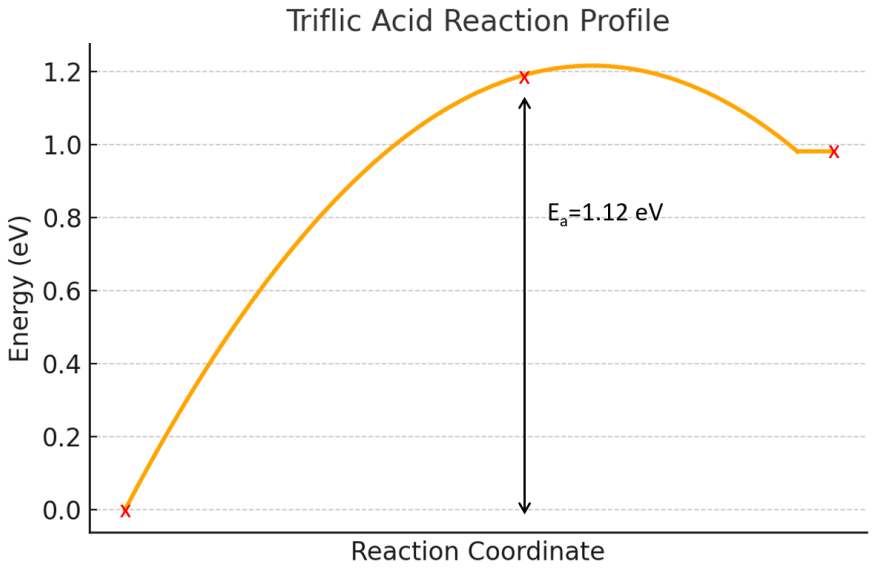

Figure 4.5: Triflic acid reaction profile

4.5. Comparison of Screened Acids with Pyrosulfated Zirconia

The comparison between the work of Jammee et al. and the screened acids in this study particularly triflic and fluorosulfiric acids is based on Lewis acidity probing, reactivity, and reaction barriers, as these are the available data from their work. Starting with Lewis acidity, Figure 1.8 shows that two probe molecules, TEPO and pyridine, were used,similar to the approach taken in this work. The interaction energies for these probes with SO_3 were reported as -2.05 eV and -1.72 eV, respectively. Among the screened acids in this work, none exhibited stronger (more negative) interaction energies compared to SO_3, indicating that SO_3 is a stronger Lewis acid. Regarding reactivity, the calculated reaction energy for SZO was -0.36 eV, which is more favorable than that of fluorosulfuric acid (-0.13 eV) obtained in this study, suggesting that SZO is more reactive. Finally, considering reaction barriers, the hydride abstraction barrier for SZO, shown in Figure 1.9, is 1.13 eV. This

value is slightly higher than the calculated barriers for both triflic acid and fluorosulfuric acid in this work, indicating that although SZO has strong acidity and high reactivity, the screened acids may offer slightly lower kinetic barriers for hydride transfer.

5

Conclusion & outlook

In this work, computational screening of main-group group based heteregeneous catalysts was done to look for potential catalysts for plastic upcycling by hydride abstraction. Adsorption energy calculation indicated that bistriflimide, phosphoric acid, boric acid, tetraboric cid exhibit interaction with the surface, while triflic acid and fluorosulfiric acid their adsorption and condensation is energy demanding. Surface saturation studies confirmed that coverage of the active sites on the surface leads to enhancement in the interaction with the surface and the effect of that is illustrated in triflic acid and fluorosulfiric acid cases .Lewis acidity was examined using TEPO, CO, and pyridine, and fluorosulfuric acid and triflic acid were found to form strong Lewis acid sites despite their weaker adsorption energies. This highlights that adsorption energy is not the sole determinant of Lewis acidity. Kinetic evaluation by NEB calculations indicated that hydride abstraction is typically endothermic for most acids, but fluorosulfuric acid is different with a slightly exothermic reaction energy. Barrier calculations were done and it was found that triflic acid and fluorosulfuric acid systems have comparable barriers with SZO. Overall, none of the screened systems surpassed SZO in Lewis acidity strength and reactivity, but triflic acid and fluorosulfuric acid have potential in future alternative catalytic designs. For recommendations, more extensive work in the future could also include expanding the scope of the screened acid species with more main-group compounds to explore potential candidates. Furthermore, replacement with larger polymer models rather than polypropylene trimer may provide a better representation of the upcycling process. Experimental testing of fluorosulfuric acid and triflic acid, would be a necessary follow-up step to confirm computational predictions. Finally, mechanistic studies beyond hydride abstraction such as β-scission and product formation pathways could be done such as the work done by Jammee et al.

Acknowledgements

Reaching this milestone would not have been possible without the support, encouragement, and guidance of many people to whom I am deeply grateful. I would first like to sincerely thank Prof. Dr. Evgeny Pidko for giving me the opportunity to do my master's thesis within the Inorganic Systems Engineering (ISE) group. I am especially thankful to my daily supervisor, Dr. Alexander Kolganov, for his continuous mentorship, patience, and invaluable advice throughout this project. His support has been fundamental to my development as a researcher. I am also incredibly grateful to my parents and friends, whose constant belief in me provided the strength to overcome challenges and remain motivated throughout this journey. Completing this thesis marks an important chapter in my academic life, and I am truly thankful for all the experiences, lessons, and people who have contributed to it.

- Amer Hassan Alramdan
Delft,april,2025

Bibliography

[1] Plastics, 11 2024. URL https://www.eea.europa.eu/en/topics/in-depth/plastics.

[2] Allan T. Williams and Nelson Rangel-Buitrago. The past, present, and future of plastic pollution. *Marine Pollution Bulletin*, 176:113429, 2 2022. doi: 10.1016/j.marpolbul.2022.113429. URL https://doi.org/10.1016/j.marpolbul.2022.113429.

[3] Plastic pollution is growing relentlessly as waste management and recycling fall short, says OECD, 2 2022. URL https://www.oecd.org/en/about/news/press-releases/2022/02/plastic-pollution-is-growing-relentlessly-as-waste-management-and-recycling-fall-short.html.

[4] Celine W. S. Yeung, Jerald Y. Q. Teo, Xian Jun Loh, and Jason Y. C. Lim. Polyolefins and polystyrene as chemical resources for a sustainable future: Challenges, advances, and Prospects. *ACS Materials Letters*, 3(12):1660–1676, 10 2021. doi: 10.1021/acsmaterialslett.1c00490. URL https://doi.org/10.1021/acsmaterialslett.1c00490.

[5] Houqian Li, Horacio A. Aguirre-Villegas, Robert D. Allen, Xianglan Bai, Craig H. Benson, Gregg T. Beckham, Sabrina L. Bradshaw, Jessica L. Brown, Robert C. Brown, Victor S. Cecon, Julia B. Curley, Greg W. Curtzwiler, Son Dong, Soumika Gaddameedi, John E. García, Ive Hermans, Min Soo Kim, Jiaze Ma, Lesli O. Mark, Manos Mavrikakis, Olumide O. Olafasakin, Tim A. Osswald, Konstantinos G. Papanikolaou, Harish Radhakrishnan, Marco Antonio Sanchez Castillo, Kevin L. Sánchez-Rivera, Khairun N. Tumu, Reid C. Van Lehn, Keith L. Vorst, Mark M. Wright, Jiayang Wu, Victor M. Zavala, Panzheng Zhou, and George W. Huber. Expanding plastics recycling technologies: chemical aspects, technology status and challenges. *Green Chemistry*, 24(23):8899–9002, 1 2022. doi: 10.1039/d2gc02588d. URL https://pubs.rsc.org/en/content/articlehtml/2022/gc/d2gc02588d.

[6] Angie F. J. Tan, Sam Yu, Cheng Wang, Guan Heng Yeoh, Wey Yang Teoh, and Alex C. K. Yip. Reimagining plastics waste as energy solutions: challenges and opportunities. *npj Materials Sustainability*, 2(1), 2 2024. doi: 10.1038/s44296-024-00007-x. URL https://doi.org/10.1038/s44296-024-00007-x.

[7] Ayesha Siddiqua, John N. Hahladakis, and Wadha Ahmed K A Al-Attiya. An overview of the environmental pollution and health effects associated with waste landfilling and open dumping. *Environmental Science and Pollution Research*, 29(39):58514–58536, 7 2022. doi: 10.1007/s11356-022-21578-z. URL https://pmc.ncbi.nlm.nih.gov/articles/PMC9399006/.

[8] Center for International Environmental Law. Plastic Climate: The Hidden Costs of a Plastic Planet - Center for International Environmental Law, 4 2022. URL https://www.ciel.org/project-update/plastic-climate-the-hidden-costs-of-a-plastic-planet/.

[9] Plastics Europe. Mechanical recycling 8226; Plastics Europe, 1 2024. URL https://plasticseurope.org/sustainability/circularity/recycling/mechanical-recycling/.

[10] Kim Ragaert, Laurens Delva, and Kevin Van Geem. Mechanical and chemical recycling of solid plastic waste. *Waste Management*, 69:24–58, 8 2017. doi: 10.1016/j.wasman.2017.07.044. URL https://doi.org/10.1016/j.wasman.2017.07.044.

[11] Shi Yin, Rabin Tuladhar, Feng Shi, Robert A. Shanks, Mark Combe, and Tony Collister. Mechanical reprocessing of polyolefin waste: A review. *Polymer Engineering and Science*, 55(12):2899–2909, 10 2015. doi: 10.1002/pen.24182. URL https://doi.org/10.1002/pen.24182.

[12] Antimo Graziano, Shaffiq Jaffer, and Mohini Sain. Review on modification strategies of polyethylene/polypropylene immiscible thermoplastic polymer blends for enhancing their mechanical behavior. *Journal of Elastomers Plastics*, 51(4):291–336, 6 2018. doi: 10.1177/0095244318783806. URL https://doi.org/10.1177/0095244318783806.

[13] Zoé O. G. Schyns and Michael P. Shaver. Mechanical Recycling of Packaging Plastics: A review. *Macromolecular Rapid Communications*, 42(3), 9 2020. doi: 10.1002/marc.202000415. URL https://doi.org/10.1002/marc.202000415.

[14] AliReza Rahimi and Jeannette M. García. Chemical recycling of waste plastics for new materials production. *Nature Reviews Chemistry*, 1(6), 6 2017. doi: 10.1038/s41570-017-0046. URL https://doi.org/10.1038/s41570-017-0046.

[15] Ina Vollmer, Michael J. F. Jenks, Mark C. P. Roelands, Robin J. White, Toon Van Harmelen, Paul De Wild, Gerard P. Van Der Laan, Florian Meirer, Jos T. F. Keurentjes, and Bert M. Weckhuysen. Beyond mechanical recycling: giving new life to plastic waste. *Angewandte Chemie International Edition*, 59(36):15402–15423, 3 2020. doi: 10.1002/anie.201915651. URL https://doi.org/10.1002/anie.201915651.

[16] Geoffrey W. Coates and Yutan D. Y. L. Getzler. Chemical recycling to monomer for an ideal, circular polymer economy. *Nature Reviews Materials*, 5(7):501–516, 4 2020. doi: 10.1038/s41578-020-0190-4. URL https://doi.org/10.1038/s41578-020-0190-4.

[17] Tian Tan, Wei Wang, Kai Zhang, Zixiang Zhan, Weiping Deng, Qinghong Zhang, and Ye Wang. Upcycling Plastic Wastes into Value Added Products by Heterogeneous Catalysis. *ChemSusChem*, 15(14), 4 2022. doi: 10.1002/cssc.202200522. URL https://doi.org/10.1002/cssc.202200522.

[18] Gabriel Perli. Chemical Recycling: Shaping a circular plastic future, 5 2024. URL https://mindthegraph.com/blog/chemical-recyling/.

[19] Daniel Hickman. Chemical versus mechanical recycling of plastic waste, 4 2022. URL https://www.chemistryviews.org/details/ezine/11222262/Chemical_Versus_Mechanical_Recycling_of_Plastic_Waste/#:~:text=Currently%2C%20companies%20are%20promoting%20chemical,not%20save%20much%20CO2.

[20] LaShanda T. J. Korley, Thomas H. Epps, Brett A. Helms, and Anthony J. Ryan. Toward polymer upcycling—adding value and tackling circularity. *Science*, 373(6550):66–69, 7 2021. doi: 10.1126/science.abg4503. URL https://doi.org/10.1126/science.abg4503.

[21] Muhammad Saad Qureshi, Anja Oasmaa, Hanna Pihkola, Ivan Deviatkin, Anna Tenhunen, Juha Mannila, Hannu Minkkinen, Maija Pohjakallio, and Jutta Laine-Ylijoki. Pyrolysis of plastic waste: Opportunities and challenges. *Journal of Analytical and Applied Pyrolysis*, 152:104804, 3 2020. doi: 10.1016/j.jaap.2020.104804. URL https://doi.org/10.1016/j.jaap.2020.104804.

[22] D. Constantinescu, Bogdan Boata, M. Iordache, M. Stelescu, M. Georgescu, and M. Sönmez. Technological considerations regarding the mechanical recycling of waste from polyethylene and polypropylene packaging. *Proceedings of the 9th International Conference on Advanced Materials and Systems*, 2022. doi: 10.24264/icams-2022.iv.3.

[23] Harish Jeswani, Christian Krüger, Manfred Russ, Maike Horlacher, Florian Antony, Simon Hann, and Adisa Azapagic. Life cycle environmental impacts of chemical recycling via pyrolysis of mixed plastic waste in comparison with mechanical recycling and energy recovery. *The Science of The Total Environment*, 769:144483, 1 2021. doi: 10.1016/j.scitotenv.2020.144483. URL https://doi.org/10.1016/j.scitotenv.2020.144483.

[24] Timmy Thiounn and Rhett C. Smith. Advances and approaches for chemical recycling of plastic waste. *Journal of Polymer Science*, 58(10):1347–1364, 4 2020. doi: 10.1002/pol.20190261. URL https://doi.org/10.1002/pol.20190261.

[25] Andreas S. Bommarius and Mariétou F. Paye. Stabilizing biocatalysts. *Chemical Society Reviews*, 42(15):6534, 1 2013. doi: 10.1039/c3cs60137d. URL https://doi.org/10.1039/c3cs60137d.

[26] Vaishali S. Shende, Vitthal B. Saptal, and Bhalchandra M. Bhanage. Recent advances utilized in the recycling of homogeneous catalysis. *The Chemical Record*, 19(9):2022–2043, 4 2019. doi: 10.1002/tcr.201800205. URL https://doi.org/10.1002/tcr.201800205.

[27] Lucas D. Ellis, Nicholas A. Rorrer, Kevin P. Sullivan, Maike Otto, John E. McGeehan, Yuriy Román-Leshkov, Nick Wierckx, and Gregg T. Beckham. Chemical and biological catalysis for plastics recycling and upcycling. *Nature Catalysis*, 4(7):539–556, 7 2021. doi: 10.1038/s41929-021-00648-4. URL https://www.nature.com/articles/s41929-021-00648-4.

[28] Daniel A. Vallero. *Control of hazardous air pollutants*. 1 2008. doi: 10.1016/b978-012373615-4/50034-0. URL https://doi.org/10.1016/b978-012373615-4/50034-0.

[29] Aakarsha Handa and Paulraj Rajamani. *Waste management and environment*. 1 2023. doi: 10.1016/b978-0-12-816109-8.00027-1. URL https://doi.org/10.1016/b978-0-12-816109-8.00027-1.

[30] Pallab Das and Pankaj Tiwari. Valorization of packaging plastic waste by slow pyrolysis. *Resources Conservation and Recycling*, 128:69–77, 10 2017. doi: 10.1016/j.resconrec.2017.09.025. URL https://doi.org/10.1016/j.resconrec.2017.09.025.

[31] Ijaz Hussain, Abdullah Aitani, Zuhair Malaibari, Hassan Alasiri, Muhammad Naseem Akhtar, Obaid Fahad Aldosari, and Shakeel Ahmed. Chemical upcycling of waste plastics to High Value-Added products via pyrolysis: Current trends, future perspectives, and Techno-Feasibility analysis. *The Chemical Record*, 23(4), 2 2023. doi: 10.1002/tcr.202200294. URL https://doi.org/10.1002/tcr.202200294.

[32] Tu Xayachak, Nawshad Haque, Raj Parthasarathy, Sarah King, Nargessadat Emami, Deborah Lau, and Biplob Kumar Pramanik. Pyrolysis for plastic waste management: An engineering perspective. *Journal of environmental chemical engineering*, 10(6):108865, 10 2022. doi: 10.1016/j.jece.2022.108865. URL https://doi.org/10.1016/j.jece.2022.108865.

[33] Rashid Miandad, Mohammad Rehan, Abdul-Sattar Nizami, Mohammad Abou El-Fetouh Barakat, and Iqbal Mohammad Ismail. *The Energy and Value-Added Products from Pyrolysis of Waste Plastics*. 1 2016. doi: 10.1007/978-981-10-0150-5\{_}12. URL https://doi.org/10.1007/978-981-10-0150-5_12.

[34] Kyong-Hwan Lee, Geug-Tae Kim, and Jeong-Gil Choi. Effect of heating rate on pyrolysis of low-grade pyrolytic oil. *Korean Journal of Chemical Engineering*, 28(6):1468–1473, 5 2011. doi: 10.1007/s11814-011-0065-x. URL https://doi.org/10.1007/s11814-011-0065-x.

[35] S.M. Al-Salem, A. Antelava, A. Constantinou, G. Manos, and A. Dutta. A review on thermal and catalytic pyrolysis of plastic solid waste (PSW). *Journal of Environmental Management*, 197:177–198, 4 2017. doi: 10.1016/j.jenvman.2017.03.084. URL https://doi.org/10.1016/j.jenvman.2017.03.084.

[36] Young-Hwa Seo, Kyong-Hwan Lee, and Dae-Hyun Shin. Investigation of catalytic degradation of high-density polyethylene by hydrocarbon group type analysis. *Journal of Analytical and Applied Pyrolysis*, 70(2):383–398, 1 2003. doi: 10.1016/s0165-2370(02)00186-9. URL https://doi.org/10.1016/s0165-2370(02)00186-9.

[37] Xianhui Zhao, Matthew Korey, Kai Li, Katie Copenhaver, Halil Tekinalp, Serdar Celik, Kyriaki Kalaitzidou, Roger Ruan, Arthur J. Ragauskas, and Soydan Ozcan. Plastic waste upcycling toward a circular economy. *Chemical Engineering Journal*, 428:131928, 8 2021. doi: 10.1016/j.cej.2021.131928. URL https://doi.org/10.1016/j.cej.2021.131928.

[38] A. López, I. De Marco, B.M. Caballero, M.F. Laresgoiti, A. Adrados, and A. Aranzabal. Catalytic pyrolysis of plastic wastes with two different types of catalysts: ZSM-5 zeolite and Red Mud. *Applied Catalysis B Environment and Energy*, 104(3-4):211–219, 4 2011. doi: 10.1016/j.apcatb.2011.03.030. URL https://doi.org/10.1016/j.apcatb.2011.03.030.

[39] Kyong-Hwan Lee. Effects of the types of zeolites on catalytic upgrading of pyrolysis wax oil. *Journal of Analytical and Applied Pyrolysis*, 94:209–214, 12 2011. doi: 10.1016/j.jaap.2011.12.015. URL https://doi.org/10.1016/j.jaap.2011.12.015.

[40] E. T. C. Vogt and B. M. Weckhuysen. Fluid catalytic cracking: recent developments on the grand old lady of zeolite catalysis. *Chemical Society Reviews*, 44(20):7342–7370, 1 2015. doi: 10.1039/c5cs00376h. URL https://doi.org/10.1039/c5cs00376h.

[41] Abdulrahman Musa, E. A. Jaseer, Samir Barman, and Nestor Garcia. Review on Catalytic Depolymerization of Polyolefin waste by Hydrogenolysis: State-of-the-Art and Outlook. *Energy Fuels*, 38(3):1676–1691, 1 2024. doi: 10.1021/acs.energyfuels.3c04109. URL https://doi.org/10.1021/acs.energyfuels.3c04109.

[42] Julie E. Rorrer, Clara Troyano-Valls, Gregg T. Beckham, and Yuriy Román-Leshkov. Hydrogenolysis of Polypropylene and Mixed Polyolefin Plastic Waste over Ru/C to Produce Liquid Alkanes. *ACS Sustainable Chemistry Engineering*, 9(35):11661–11666, 7 2021. doi: 10.1021/acssuschemeng.1c03786. URL https://doi.org/10.1021/acssuschemeng.1c03786.

[43] Mehdi Zare, Pavel A. Kots, Zachary R. Hinton, Thomas H. Epps, LaShanda T.J. Korley, Stavros Caratzoulas, and Dionisios G. Vlachos. Effect of reaction media on hydrogenolysis of polyethylene plastic waste: Polymer-surface interactions in small alkane/polymer blends. *Applied Catalysis B Environment and Energy*, 351:123969, 4 2024. doi: 10.1016/j.apcatb.2024.123969. URL https://doi.org/10.1016/j.apcatb.2024.123969.

[44] Linxiao Chen, Yifeng Zhu, Laura C. Meyer, Lillian V. Hale, Thuy T. Le, Abhi Karkamkar, Johannes A. Lercher, Oliver Y. Gutiérrez, and János Szanyi. Effect of reaction conditions on the hydrogenolysis of polypropylene and polyethylene into gas and liquid alkanes. *Reaction Chemistry Engineering*, 7(4):844–854, 1 2022. doi: 10.1039/d1re00431j. URL https://doi.org/10.1039/d1re00431j.

[45] Pavel A. Kots, Tianjun Xie, Brandon C. Vance, Caitlin M. Quinn, Matheus Dorneles De Mello, J. Anibal Boscoboinik, Cong Wang, Pawan Kumar, Eric A. Stach, Nebojsa S. Marinkovic, Lu Ma, Steven N. Ehrlich, and Dionisios G. Vlachos. Electronic modulation of metal-support interactions improves polypropylene hydrogenolysis over ruthenium catalysts. *Nature Communications*, 13(1), 9 2022. doi: 10.1038/s41467-022-32934-5. URL https://www.nature.com/articles/s41467-022-32934-5.

[46] Ratchawi Jammee, Alexander Kolganov, Marc C Groves, Evgeny A Pidko, Evgeny Pidko, Orson L Sydora, and Matthew Conley. C-H Bond Activation by Sulfated Zirconium Oxide is Mediated by a Sulfur-Centered Lewis Superacid. *Angewandte Chemie International Edition*, 12 2024. doi: 10.1002/anie.202421699. URL https://doi.org/10.1002/anie.202421699.

[47] Hajar Hosseini, Connor J. Herring, Chukwudi F. Nwaokorie, Gloria A. Sulley, and Matthew M. Montemore. Computational Design of Catalysts with Experimental Validation: Recent Successes, Effective Strategies, and Pitfalls. *The Journal of Physical Chemistry C*, 128(43):18144–18157, 10 2024. doi: 10.1021/acs.jpcc.4c04949. URL https://doi.org/10.1021/acs.jpcc.4c04949.

[48] None Shambhawi, Ojus Mohan, Tej S. Choksi, and Alexei A. Lapkin. The design and optimization of heterogeneous catalysts using computational methods. *Catalysis Science Technology*, 14(3):515–532, 12 2023. doi: 10.1039/d3cy01160g. URL https://pubs.rsc.org/en/content/articlehtml/2024/cy/d3cy01160g.

[49] David S. Sholl and Janice A. Steckel. *Density Functional Theory*. 3 2009. doi: 10.1002/9780470447710. URL https://doi.org/10.1002/9780470447710.

[50] Wolfram Koch and Max C. Holthausen. *A Chemist's Guide to Density Functional Theory*. 7 2001. doi: 10.1002/3527600043. URL https://doi.org/10.1002/3527600043.

[51] Walter Kohn and Lu Jeu Sham. Self-consistent equations including exchange and correlation effects. *Physical Review*, 140(4A):A1133, 1965. doi: 10.1103/PhysRev.140.A1133.

[52] Benjamin W. J. Chen, Lang Xu, and Manos Mavrikakis. Computational methods in heterogeneous catalysis. *Chemical Reviews*, 121(2):1007–1048, 12 2020. doi: 10.1021/acs.chemrev.0c01060. URL https://doi.org/10.1021/acs.chemrev.0c01060.

[53] Soumen Ghosh, Pragya Verma, Christopher J. Cramer, Laura Gagliardi, and Donald G. Truhlar. Combining Wave Function Methods with Density Functional Theory for Excited States. *Chemical Reviews*, 118(15):7249–7292, 7 2018. doi: 10.1021/acs.chemrev.8b00193. URL https://doi.org/10.1021/acs.chemrev.8b00193.

[54] Sarah A. Tolba, Kareem M. Gameel, Basant A. Ali, Hossam A. Almossalami, and Nageh K. Allam. *The DFT+U: Approaches, Accuracy, and Applications*. 5 2018. doi: 10.5772/intechopen.72020. URL https://doi.org/10.5772/intechopen.72020.

[55] Hendrik J. Monkhorst and James D. Pack. Special points for Brillouin-zone integrations. *Physical review. B, Solid state*, 13(12):5188–5192, 6 1976. doi: 10.1103/physrevb.13.5188. URL https://doi.org/10.1103/physrevb.13.5188.

[56] Errol G. Lewars. *The concept of the potential energy surface*. 9 2010. doi: 10.1007/978-90-481-3862-3\{_}2. URL https://doi.org/10.1007/978-90-481-3862-3_2.

[57] Neil Hunt. Lecture 4: Potential energy surfaces. https://www.huntresearchgroup.org.uk/teaching/teaching_comp_chem_year4/L4_PES.pdf, 2020. Accessed: 2025-04-01.

[58] Albert Y. S. Lam and Victor O. K. Li. Chemical Reaction Optimization: a tutorial. *Memetic Computing*, 4 (1):3–17, 2 2012. doi: 10.1007/s12293-012-0075-1. URL https://doi.org/10.1007/s12293-012-0075-1.

[59] Janice Lan, Aini Palizhati, Muhammed Shuaibi, Brandon M. Wood, Brook Wander, Abhishek Das, Matt Uyttendaele, C. Lawrence Zitnick, and Zachary W. Ulissi. AdsorbML: a leap in efficiency for adsorption energy calculations using generalizable machine learning potentials. *npj Computational Materials*, 9 (1), 9 2023. doi: 10.1038/s41524-023-01121-5. URL https://www.nature.com/articles/s41524-023-01121-5.

[60] John P. Osegovic and Russell S. Drago. A solid acidity scale based on the31P MAS-NMR shift of chemisorbed triethylphosphine oxide. *Journal of Catalysis*, 182(1):1–4, 2 1999. doi: 10.1006/jcat.1998.2393. URL https://doi.org/10.1006/jcat.1998.2393.

[61] Zita Huesges, Carsten Müller, Beate Paulus, Christine Hough, Nicholas Harrison, and Erhard Kemnitz. Characterising MgF2 surfaces with CO adsorption calculations. *Surface Science*, 609:73–77, 11 2012. doi: 10.1016/j.susc.2012.11.004. URL https://doi.org/10.1016/j.susc.2012.11.004.

[62] Donat-Pierre Luigi. NMR and Theoretical Study of Acidity Probes on Sulfated Zirconia Catalysts. *chrisspreckley*, 1 2000. URL https://www.academia.edu/81990389/NMR_and_Theoretical_Study_of_Acidity_Probes_on_Sulfated_Zirconia_Catalysts.

[63] Init.At. VASP - Vienna Ab initio Simulation Package. URL https://www.vasp.at/.

[64] John P. Perdew, Kieron Burke, and Matthias Ernzerhof. Generalized gradient approximation made simple. *Physical Review Letters*, 77(18):3865–3868, 1996. doi: 10.1103/PhysRevLett.77.3865.

[65] Alexander Hofmann, Stewart J. Clark, Markus Oppel, and Ina Hahndorf. Hydrogen adsorption on the tetragonal ZrO2(101) surface: a theoretical study of an important catalytic reactantElectronic supplementary information (ESI) available: data for geometrical and charge differences in detail. See http://www.rsc.org/suppdata/cp/b2/b202330j/. *Physical Chemistry Chemical Physics*, 4(14):3500–3508, 6 2002. doi: 10.1039/b202330j. URL https://pubs.rsc.org/en/content/articlelanding/2002/cp/b202330j.

[66] Frank Haase and Joachim Sauer. The Surface Structure of Sulfated Zirconia: Periodic ab Initio Study of Sulfuric Acid Adsorbed on ZrO2(101) and ZrO2(001). *Journal of the American Chemical Society*, 120(51):13503–13512, 12 1998. doi: 10.1021/ja9825534. URL https://doi.org/10.1021/ja9825534.

[67] Snellius: de Nationale Supercomputer. URL https://www.surf.nl/diensten/snellius-de-nationale-supercomputer.

[68] Rachid Masrour. *Computational methods: AB initio calculations and Monte Carlo simulations*. 1 2023. doi: 10.1007/978-3-031-40613-3\{_}2. URL https://doi.org/10.1007/978-3-031-40613-3_2.

[69] El-Sayed R. Khattab, Sayed S. Abd El Rehim, Walid M. I. Hassan, and Tamer S. El-Shazly. Band structure engineering and optical Properties of pristine and doped monoclinic zirconia (M-ZRO2): Density Functional Theory Theoretical Prospective. *ACS Omega*, 6(44):30061–30068, 10 2021. doi: 10.1021/acsomega.1c04756. URL https://doi.org/10.1021/acsomega.1c04756.

[70] Chemcraft - Graphical program for visualization of quantum chemistry computations. URL https://www.chemcraftprog.com/.

[71] SCM. Documentation - SCM, 7 2024. URL https://www.scm.com/doc/AMS/Tasks/NEB.html.

[72] Graeme Henkelman, Blas P. Uberuaga, and Hannes Jónsson. A climbing image nudged elastic band method for finding saddle points and minimum energy paths. *The Journal of Chemical Physics*, 113(22): 9901–9904, 12 2000. doi: 10.1063/1.1329672. URL https://doi.org/10.1063/1.1329672.

[73] Materials square. [MatSQ Tip] Module Utilization Tip: Nudged Elastic Band, 9 2020. URL https://www.materialssquare.com/blog/matsq-tip-neb-en.

Appendices contents

A Varying proton locations 1
- A.1 Coloring scheme . . . 1
- A.2 Pyrophosphate on ZrO_2 . . . 1
- A.3 Tetraboric acid on ZrO_2 . . . 2
- A.4 Diboric acid on ZrO_2 . . . 3
- A.5 Disulfuryl fluoride, Triflic acid anhydride, and Bistriflimide on ZrO_2 . . . 3
- A.6 Adsorption energies . . . 4

B Surface saturation 5
- B.1 Coloring scheme . . . 5
- B.2 Phosphoric acid . . . 5
- B.3 Tetraboric acid . . . 6
- B.4 Boric acid . . . 6
- B.5 Fluorosulfuric acid . . . 6
- B.6 Triflic acid . . . 7
- B.7 Bistriflimide . . . 7
- B.8 Effect of surface saturation . . . 8

C Reactivity 9
- C.1 Coloring scheme . . . 9
- C.2 Phosphoric acid . . . 9
- C.3 Tetraboric acid . . . 10
- C.4 Boric acid . . . 10
- C.5 Fluorosulfuric acid . . . 11
- C.6 Triflic acid . . . 11
- C.7 Tetraboric acid (reorganized) . . . 12
- C.8 Reaction energies . . . 12

D Probing lewis acids 13
- D.1 Coloring scheme . . . 13
- D.2 Phosphoric acid . . . 13
- D.3 Tetraboric acid . . . 14
- D.4 Boric acid . . . 14
- D.5 Fluorosulfuric acid . . . 15
- D.6 Triflic acid . . . 15

E Artificial Intelligence 16
- E.1 Literture search . . . 16
- E.2 Language Refinement and Scientific Writing Assistance . . . 16
- E.3 Scientific Concept Clarification . . . 17
- E.4 Scripting and Automation . . . 17

F INCAR tags 18

A

Varying proton locations

A.1. Coloring scheme

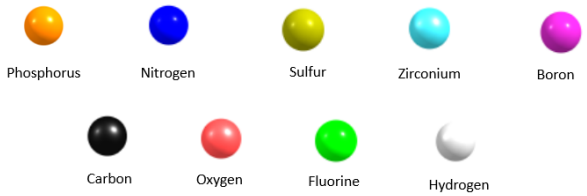

Figure A.1: Colouring scheme used in the presentation of structures.

A.2. Pyrophosphate on ZrO_2

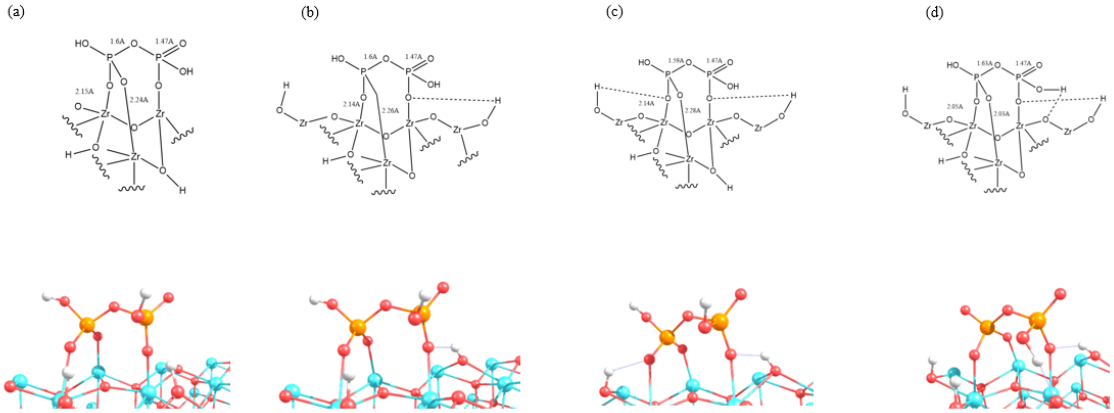

Figure A.2: Varying proton locations for pyrophosphate adsorbed on the ZrO_2 surface. The top row shows schematic representations with bond lengths (Å), while the bottom row presents corresponding 3D structures.

Table A.1: Relative energies for different configurations.

Configuration	Relative energy (eV)
a (reference)	0
b	0.40
c	0.92
d	0.75

A.3. Tetraboric acid on ZrO_2

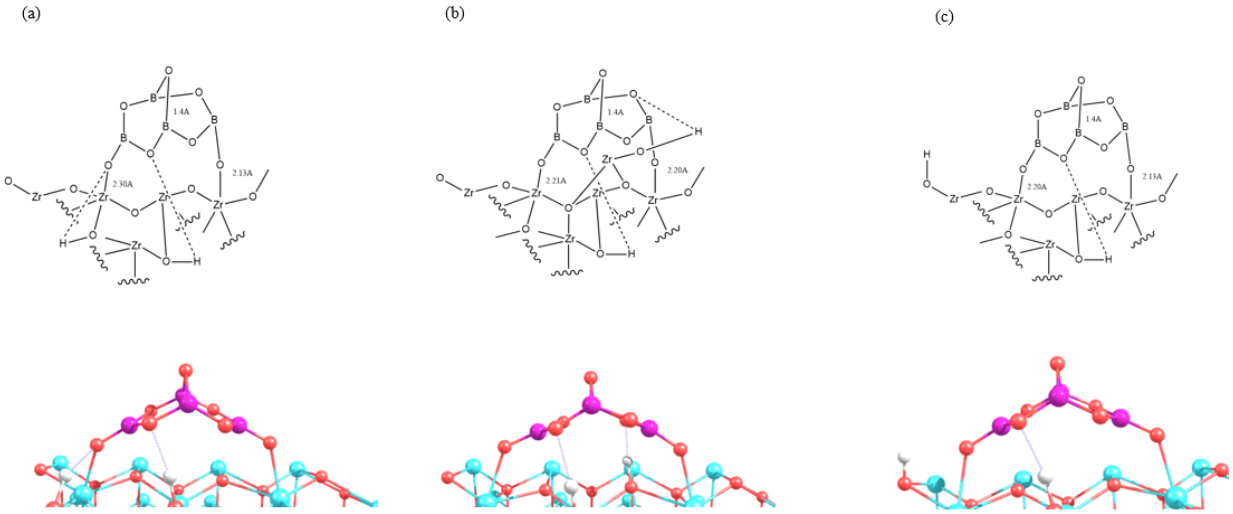

Figure A.3: Varying proton locations for tetraboric acid adsorbed on the ZrO_2 surface. The top row shows schematic representations with bond lengths (Å), while the bottom row presents corresponding 3D structures.

Table A.2: Relative energies for different configurations.

Configuration	Relative energy (eV)
a (reference)	0
b	0.95
c	0.44

Configuration 1 is the most stable, followed by Configuration 3, which is more stable than Configuration 2, the least stable of the three.

A.4. Diboric acid on ZrO_2

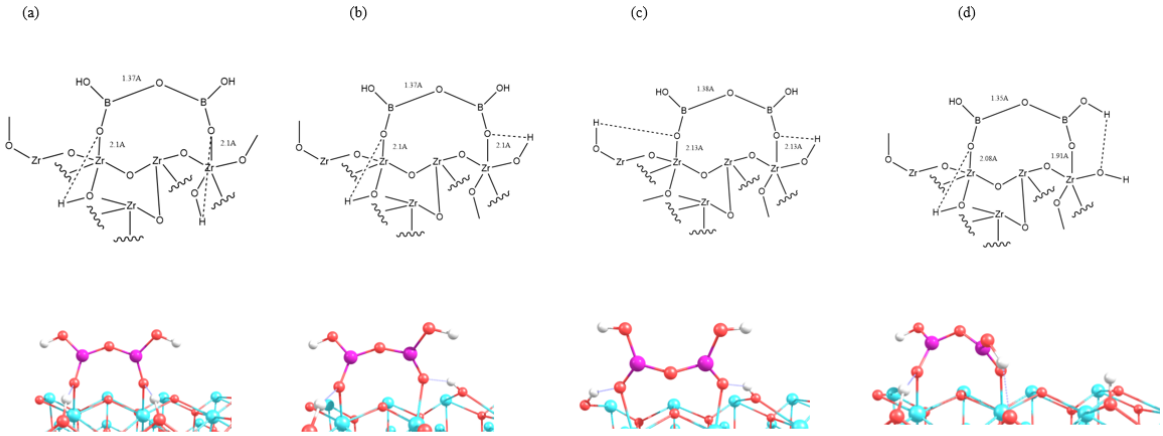

Figure A.4: Varying proton locations for diboric acid adsorbed on the ZrO_2 surface. The top row shows schematic representations with bond lengths (Å), while the bottom row presents corresponding 3D structures.

Table A.3: Relative energies of different configurations.

Configuration	Relative energy (eV)
a (reference)	0
b	0.54
c	1.15
d	0.68

Configuration 1 is the most stable. Configuration 3 is the least stable, as the configuration has protons positioned farther from favorable coordination sites. Configurations 2 and 4 show intermediate stability.

A.5. Disulfuryl fluoride, Triflic acid anhydride, and Bistriflimide on ZrO_2

For Disulfuryl Fluoride and Triflic Acid Anhydride both molecules are in their dehydrated forms, and there is no proton present on the surface that can be varied. For Bistriflimide, only one hydrogen atom is present.

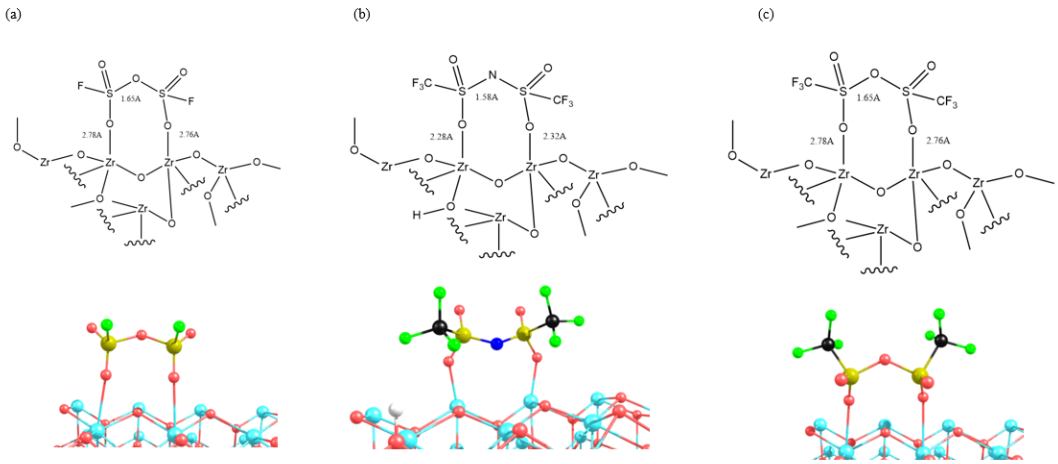

Figure A.5: structure of (a) Disulfuryl fluoride, (b) Triflic acid anhydride, and (c) Bistriflimide on ZrO_2. The top row shows schematic representations with bond lengths (Å), while the bottom row presents corresponding 3D structures.

A.6. Adsorption energies

Table A.4: Dehydration reactions and adsorption energy values for various molecules on the ZrO_2 surface.

Molecule	Dehydration	Adsorption energy (eV)
H_3PO_4	$ZrO_2 + 2H_3PO_4 \longrightarrow H_2P_2O_7, 2H/ZrO_2 + H_2O$	-4.53
$H_2B_4O_7$	$ZrO_2 + H_2B_4O_7 \longrightarrow H_2B_4O_7, 2H/ZrO_2$	-0.05
H_3BO_3	$ZrO_2 + 2H_3BO_3 \longrightarrow H_2B_2O_5, 2H/ZrO_2 + H_2O$	-2.56
$HSFO_3$	$ZrO_2 + 2HSFO_3 \longrightarrow S_2O_5F_2/ZrO_2 + H_2O$	0.26
HCF_3SO_3	$ZrO_2 + 2CF_3SO_3H \longrightarrow (CF_3SO_2)_2O/ZrO_2 + H_2O$	0.13
$(CF_3SO_2)_2NH$	-	-2.40

Note: When calculating the adsorption energies, stoichiometry must be taken into account. For example, for phosphoric acid (H_3PO_4), the adsorption energy is calculated using the following equation:

$$\text{Adsorption Energy (eV)} = E_{\text{total}} + E_{\text{H2O(g)}} - E_{\text{surface}} - 2 \times E_{\text{H3PO4(g)}} \tag{A.1}$$

This formula considers the total energy (E_{total}) of the system after adsorption, the energy of water ($E_{\text{H2O(g)}}$) in the gas phase, the energy of the surface (E_{surface}), and the energy of two molecules of phosphoric acid ($E_{\text{H3PO4(g)}}$) in the gas phase. Similar equations are used for the other molecules as per the dehydration reactions.

B

Surface saturation

As mentioned before in section 3.3 to make use of the surface, dimeric species, in addition to active acid species were adsorbed onto the surface to simulate real conditions.

B.1. Coloring scheme

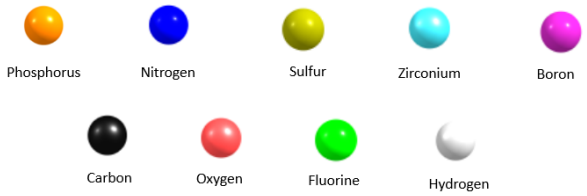

Figure B.1: Colouring scheme used in the presentation of structures.

B.2. Phosphoric acid

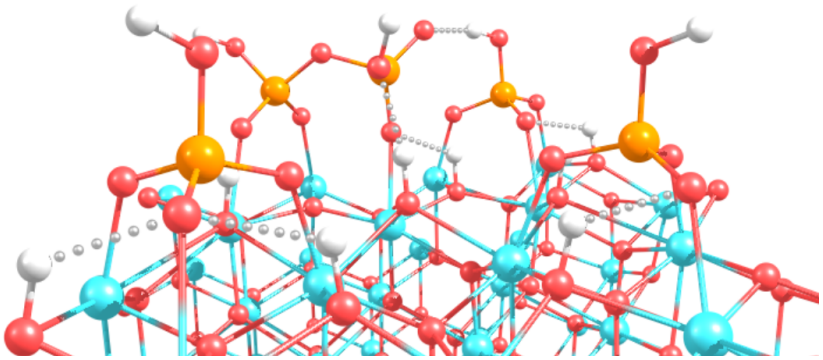

Figure B.2: Saturation of pyrophosphated zicronia. Three $HPO_4{}^{2-}$ species were added, leading to eight total surface protons.

B.3. Tetraboric acid

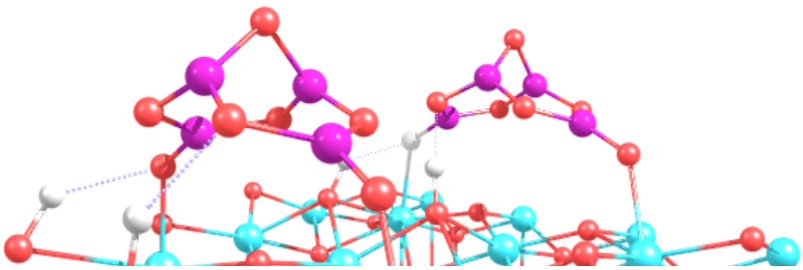

Figure B.3: one additional tetraboric was adsorbed, leading to four total surface protons.

B.4. Boric acid

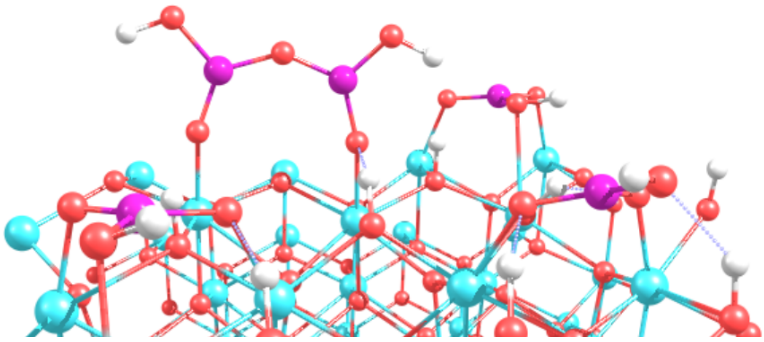

Figure B.4: saturation of diboric acid on ZrO_2. Three $HBO_3{}^{2-}$ species were added, leading to eight total surface protons.

B.5. Fluorosulfuric acid

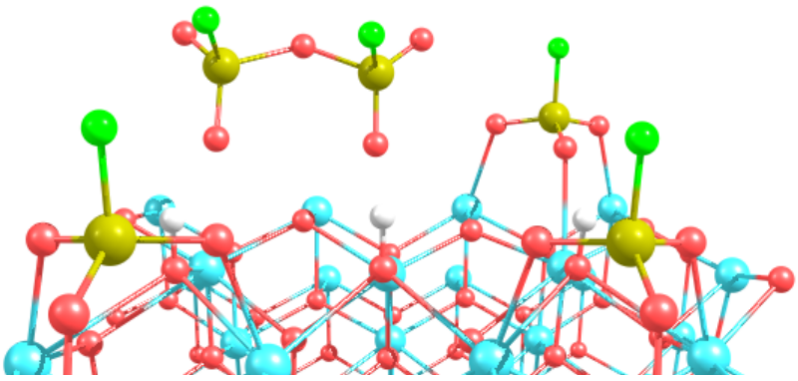

Figure B.5: saturation of disulfuryl fluoride on ZrO_2. Three $SFO_3{}^-$ species were added, leading to three total surface protons.

B.6. Triflic acid

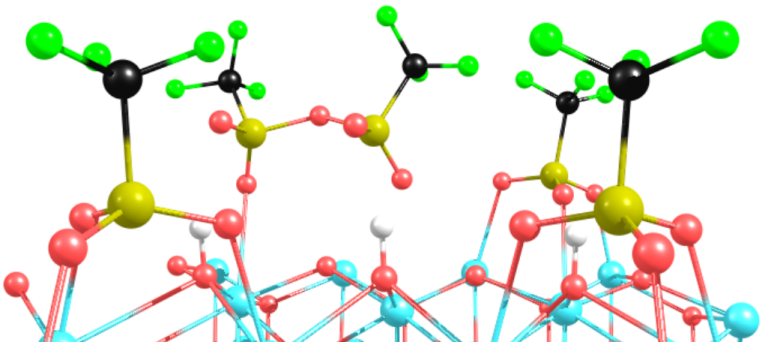

Figure B.6: saturation of triflic anhydride on ZrO_2. Three $CF_3SO_3^-$ species were added, leading to three total surface protons.

B.7. Bistriflimide

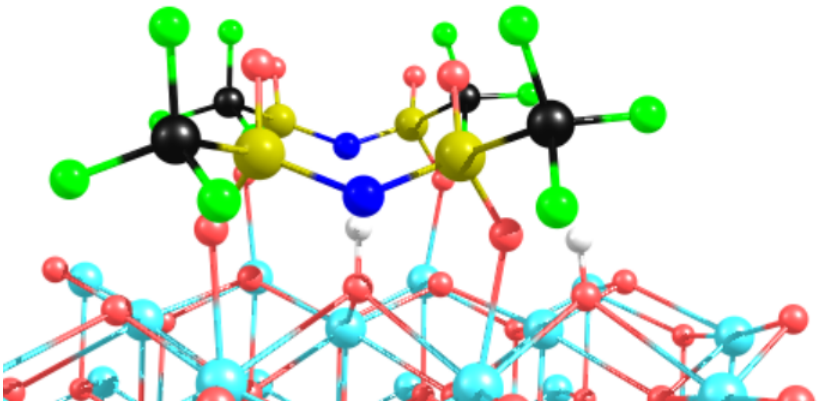

Figure B.7: one additional bistriflimide was adsorbed, leading to two surface protons.

B.8. Effect of surface saturation

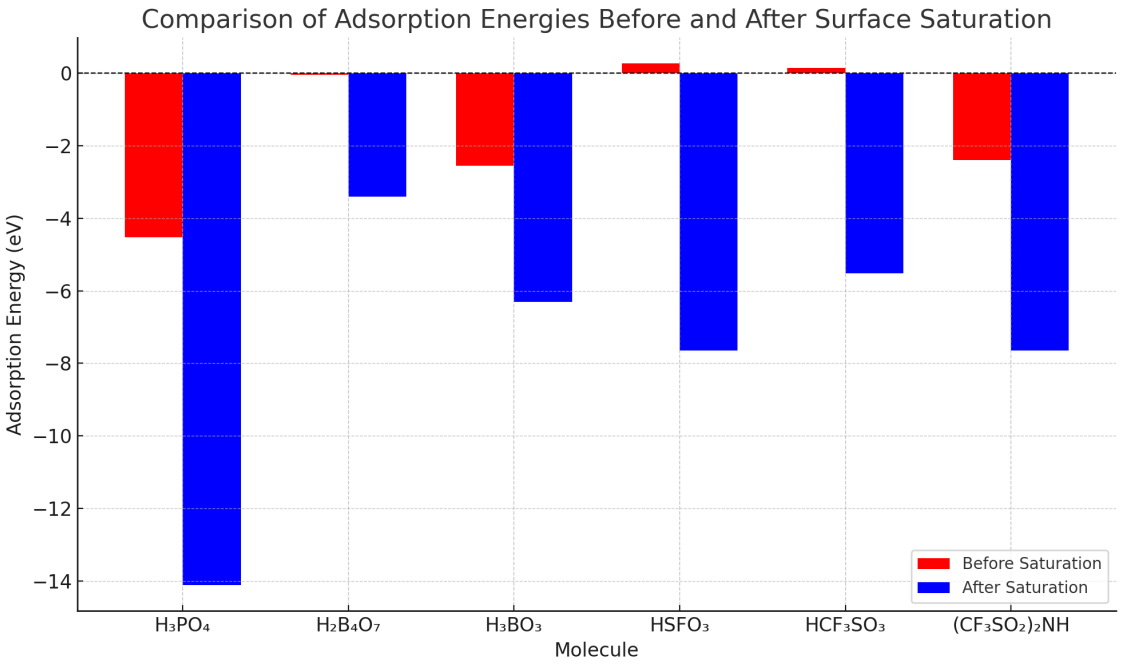

Figure B.8: Adsorption energies (eV) of various acids before (red) and after (blue) surface saturation.

C

Reactivity

C.1. Coloring scheme

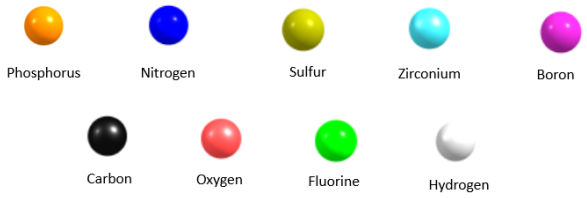

Figure C.1: Colouring scheme used in the presentation of structures.

C.2. Phosphoric acid

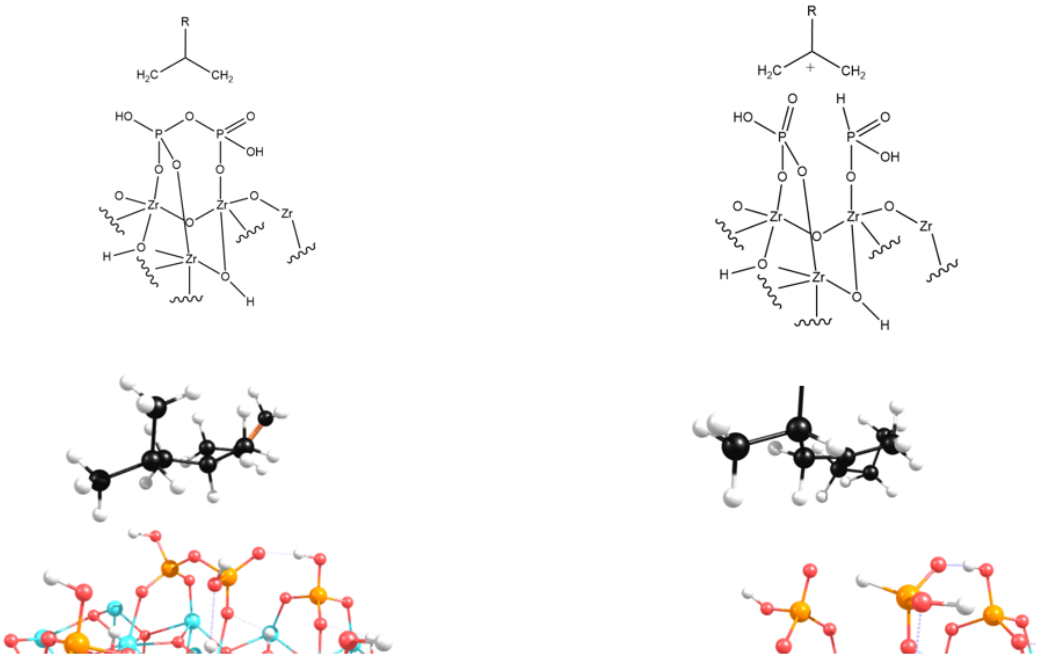

Figure C.2: (Left) Initial state with trimer on top. (Right) Final state after hydride abstraction.

C.3. Tetraboric acid

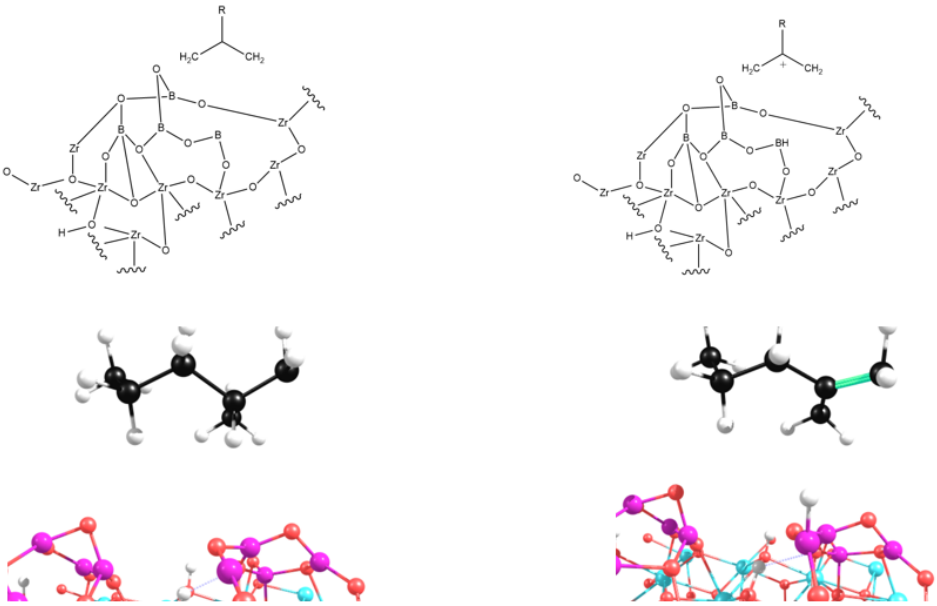

Figure C.3: (Left) Initial state with trimer on top. (Right) Final state after hydride abstraction.

C.4. Boric acid

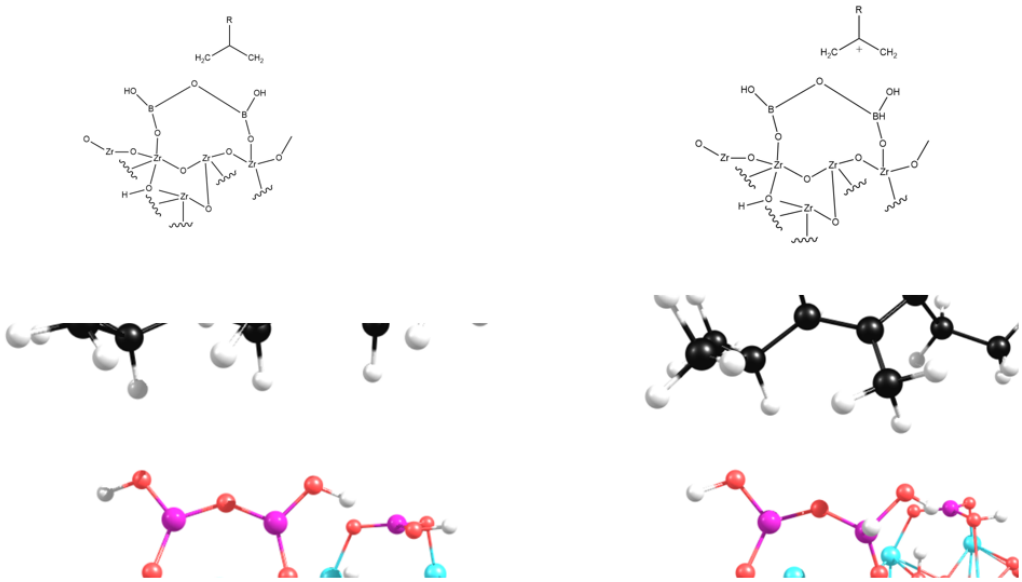

Figure C.4: (Left) Initial state with trimer on top. (Right) Final state after hydride abstraction.

C.5. Fluorosulfuric acid

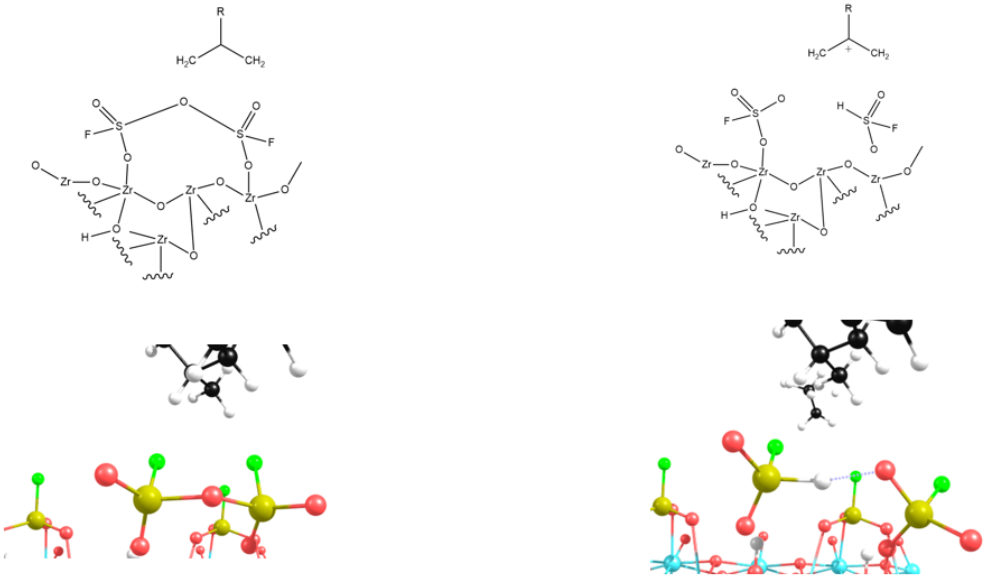

Figure C.5: (Left) Initial state with trimer on top. (Right) Final state after hydride abstraction.

C.6. Triflic acid

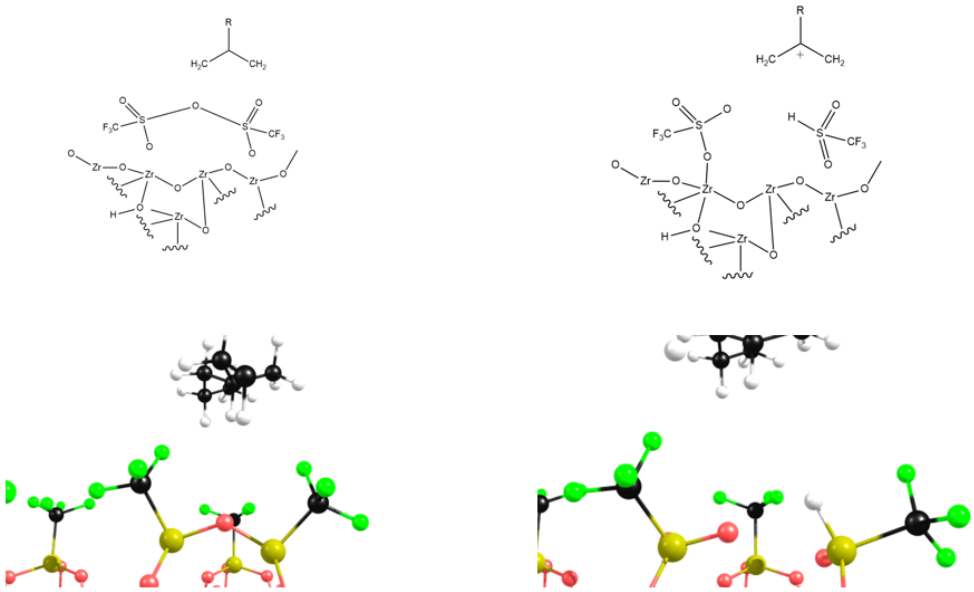

Figure C.6: (Left) Initial state with trimer on top. (Right) Final state after hydride abstraction.

C.7. Tetraboric acid (reorganized)

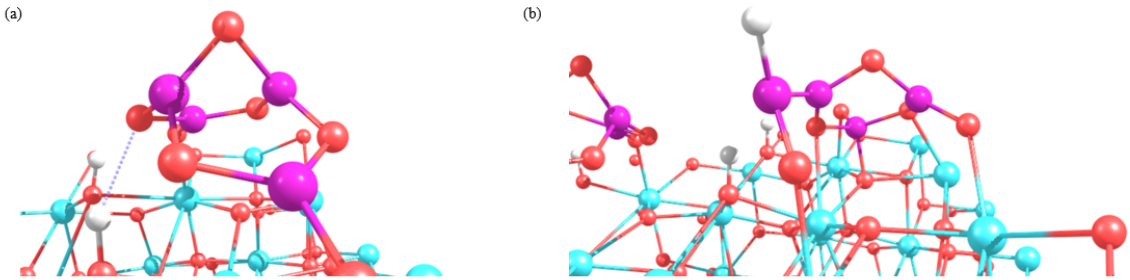

Figure C.7: (a) Tetraborate (B_4O_7) remains intact. (b) Zr and O sites are more exposed. Borate cluster is distorted. Borate shifts downward, forming new Zr-O coordination.

C.8. Reaction energies

Table C.1: Computed reaction energies after hydride abstraction for each acid. Energies are given as total electronic values (E1 and E2) and their differences reaction energies.

Molecule	**E1 (Before Transfer)**	**E2 (After Transfer)**	**Reaction Energy (eV)**
H_3PO_4	-1663.37	-1662.24	1.13
H_3BO_3	-1632	-1627.68	4.32
HSO_3F	-1583.94	-1584.06	-0.13
HCF_3SO_3	-1667.47	-1666.69	0.78
$H_2B_4O_7$ (Reorganized)	-1622.36	-1620.77	1.6

D

Probing lewis acids

D.1. Coloring scheme

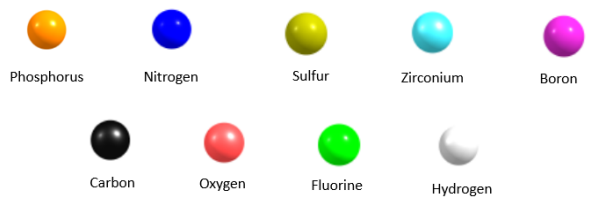

Figure D.1: Colouring scheme used in the presentation of structures.

D.2. Phosphoric acid

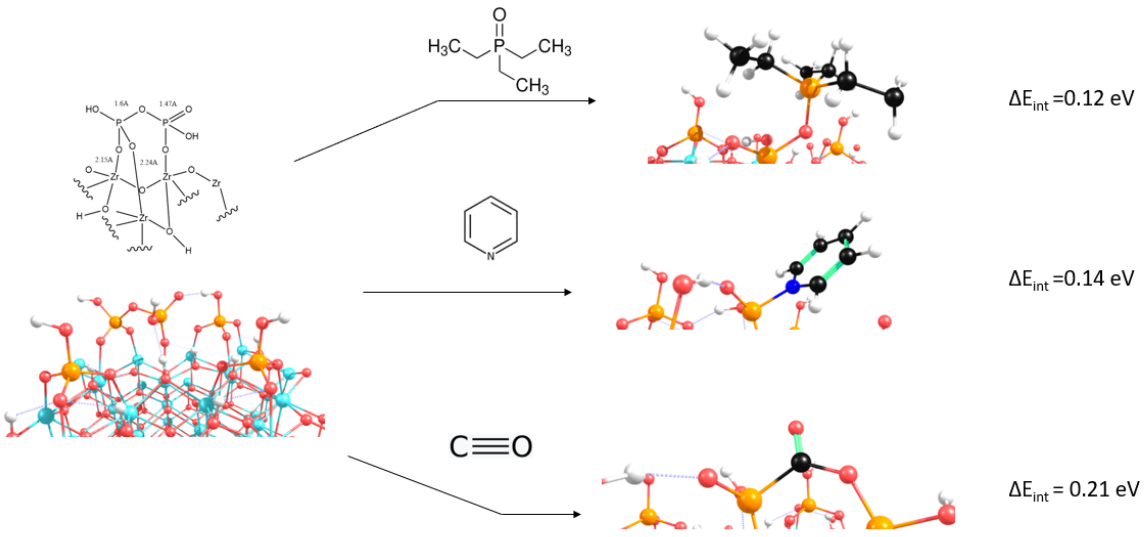

Figure D.2: Interaction of lewis acid with Tepo,Pyridine,CO

D.3. Tetraboric acid

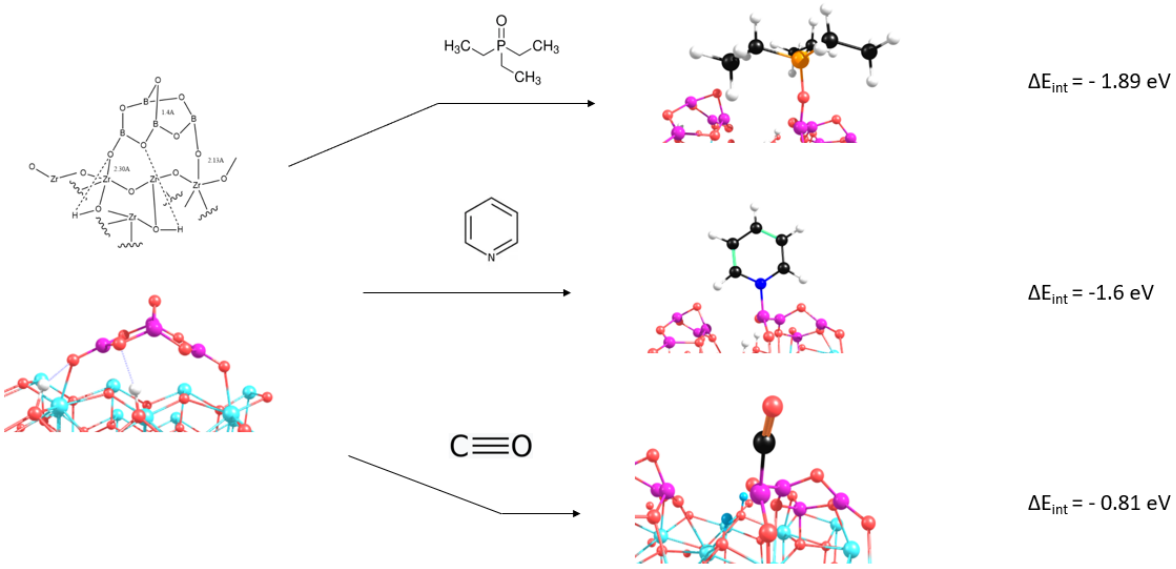

Figure D.3: Interaction of lewis acid with Tepo,Pyridine,CO

D.4. Boric acid

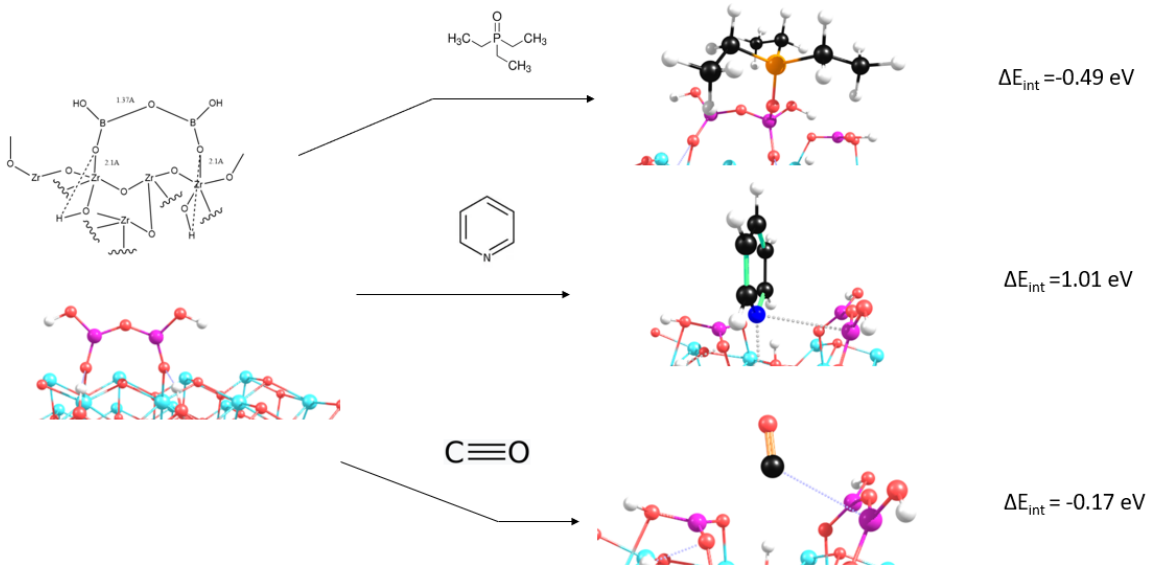

Figure D.4: Interaction of lewis acid with Tepo,Pyridine,CO

D.5. Fluorosulfuric acid

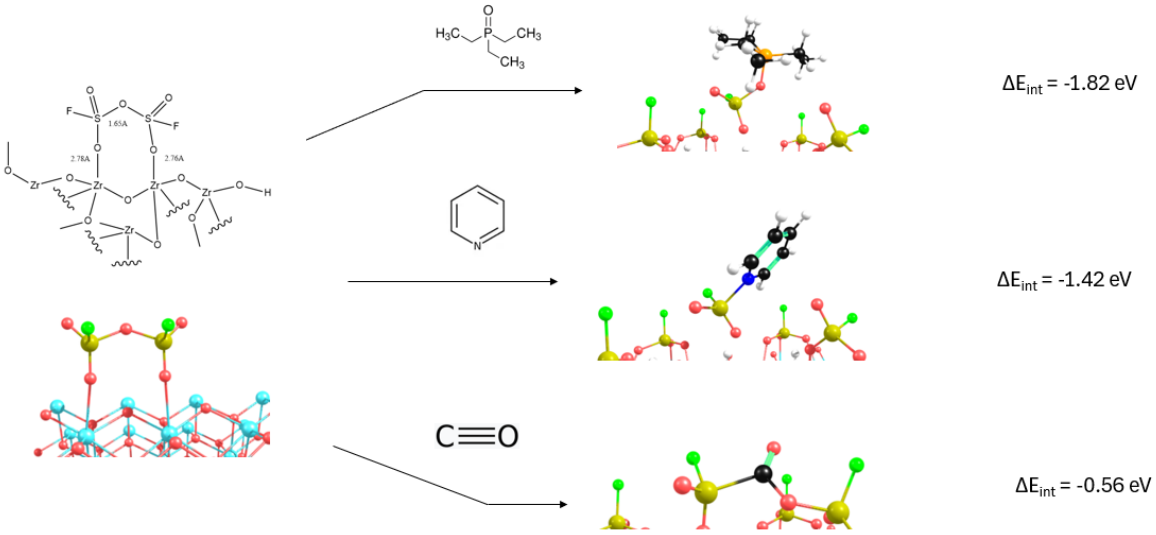

Figure D.5: Interaction of lewis acid with Tepo,Pyridine,CO

D.6. Triflic acid

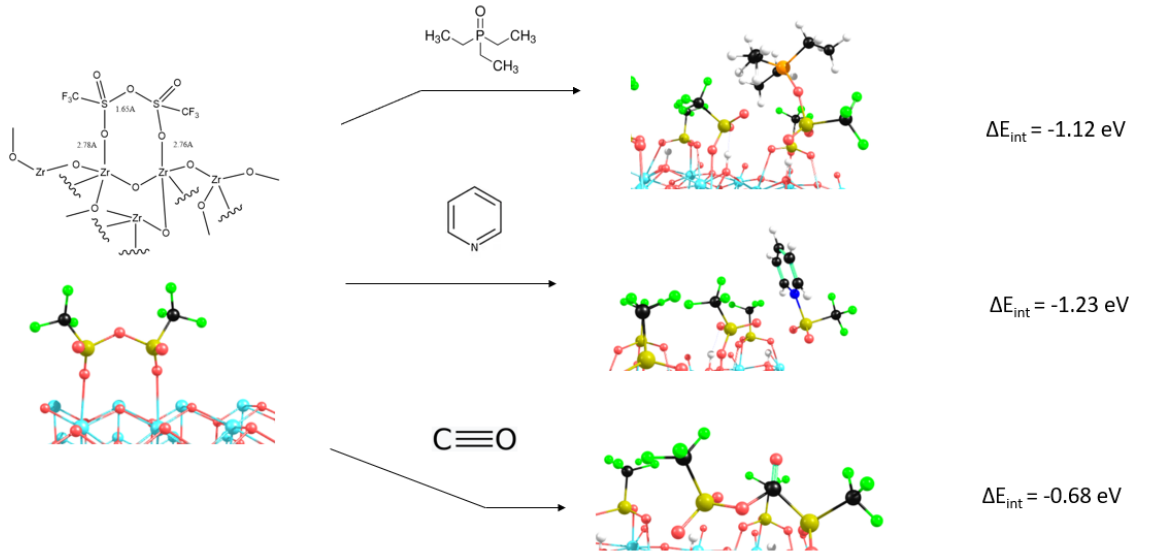

Figure D.6: Interaction of lewis acid with Tepo,Pyridine,CO

E

Artificial Intelligence

Throughout the writing of this thesis, artificial intelligence (AI) tools (e.g., ChatGPT) were used to support various aspects of the work. These tools were used for literature searches, text paraphrasing for clarity, grammar checking, evaluating the logical flow of writing, explaining scientific concepts, assisting with Python scripts for data handling, and generating LaTeX code for formatting and writing.

E.1. Literture search

In cases where the relevant literature was difficult to locate through traditional academic databases, AI tools were used to support the search process. Specifically, platforms such as Consensus were used to extract insights. All references included in this thesis were manually reviewed to ensure their scientific validity and relevance.

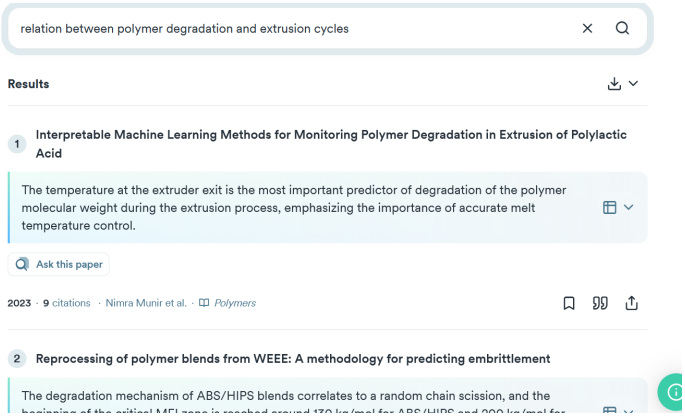

Figure E.1: Example of using consensus for literature search.

E.2. Language Refinement and Scientific Writing Assistance

To improve the clarity and readability of the thesis, AI tools such as ChatGPT and Grammarly were employed for paraphrasing and restructuring technical content. These tools helped rephrase complex ideas into concise and coherent language. In addition to paraphrasing, they were used to check grammar, sentence structure, and the overall logical flow of the text. Furthermore, ChatGPT assisted in generating LaTeX code for figures, tables, and mathematical expressions, contributing to efficient and consistent document preparation.

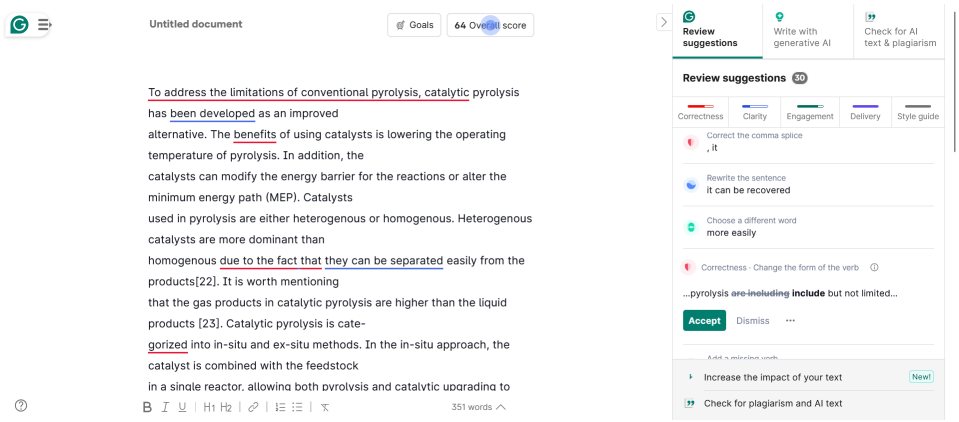

Figure E.2: Grammarly interface showing grammar and clarity suggestions.

E.3. Scientific Concept Clarification

Since understanding complex scientific concepts can be time-consuming, ChatGPT were used to assist in clarifying challenging topics during the writing process. These tools provided quick and accessible explanations, which helped improve comprehension. However, as ChatGPT can occasionally provide inaccurate or contradictory information, its outputs were always critically evaluated and cross-checked with relevant literature to ensure accuracy and reliability.

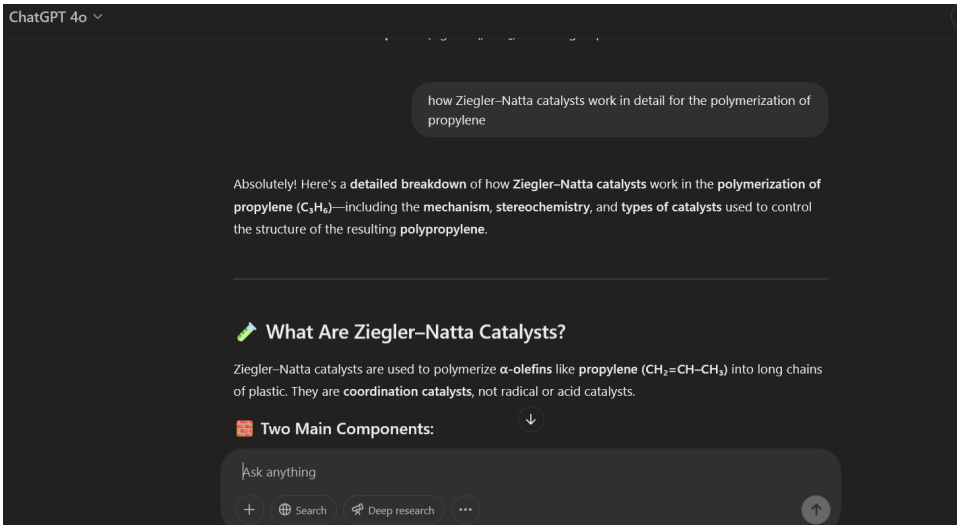

Figure E.3: Exmaple of using Chatgpt to simplify and explain scientific concepts.

E.4. Scripting and Automation

Python was employed throughout the project to automate various repetitive tasks and improve workflow efficiency. In particular, Python scripts were developed to construct POSCAR files for VASP simulations by arranging atomic coordinates and assigning selective dynamics tags in next to the coordinates as shown in figure 3.1.

F

INCAR tags

Table F.1: Summary of INCAR parameters used in VASP calculations.

Electronic Relaxation Parameters		
ENCUT	550.0 eV	Plane-wave energy cutoff.
EDIFF	1×10^{-5}	Electronic SCF convergence criterion.
LREAL	Auto	Real or reciprocal space determined automatically.
NELMIN	8	Minimum number of electronic steps.
ALGO	Fast	RMM-DIIS electronic minimization algorithm.
DFT+U Settings		
LDAU	TRUE	Enables Hubbard U correction.
LDAUTYPE	2	Dudarev's simplified rotationally invariant approach.
LDAUL	-1 -1 -1 -1 2	Angular momentum for main group elements are -1. 2 is applied to d orbitals of Zr
LDAUU	0.00 0.00 0.00 0.00 4.00	strength of the effective on-site Coulomb interactions. only applied to Zr
LMAXMIX	4	Maximum l-quantum number for mixing; needed for d orbitals.
Ionic Relaxation Parameters		
EDIFFG	0.04	break condition for the ionic relaxation loop
ISIF	2	Only position degrees of freedom are al; keeps cell volume and shape fixed.
NSW	500	number of ionic steps.
IBRION	3	Damped molecular dynamics
POTIM	0	Time step for ionic motion (used with IOPT = 7).
IOPT	7	Quasi-Newton optimization algorithm.